UNIVERSIDAD DE CHILE
FACULTAD DE CIENCIAS FÍSICAS Y MATEMÁTICAS
DEPARTAMENTO DE INGENIERÍA ELÉCTRICA

CHANNEL MODELING IN IOT DEPLOYMENTS SUPPORTED BY LEO NANOSATELLITES

TESIS PARA OPTAR AL GRADO DE MAGISTER EN CIENCIAS DE LA INGENIERÍA, MENCIÓN ELÉCTRICA

MEMORIA PARA OPTAR AL TÍTULO DE INGENIERO CIVIL ELÉCTRICO

TOMÁS BENJAMÍN NÚÑEZ GONZÁLEZ

PROFESOR GUÍA:
CESAR AZURDIA MEZA

PROFESORA CO-GUÍA:
SANDRA CÉSPEDES UMAÑA

MIEMBROS DE LA COMISIÓN:
JORGE SILVA SÁNCHEZ
CARLOS GUTIERREZ DIAZ DE LEÓN

Este trabajo ha sido parcialmente financiado por Proyecto FONDECYT Regular 1201893, Program STIC-AMSUD STIC2020003 Folio 21-STIC-12, y Beca Magíster Nacional ANID Folio 22210143.

SANTIAGO DE CHILE
2022

RESUMEN DE LA TESIS PARA OPTAR AL GRADO DE
MAGISTER EN CIENCIAS DE LA INGENIERÍA,
MENCIÓN ELÉCTRICA
Y MEMORIA PARA OPTAR AL TÍTULO DE
INGENIERO CIVIL ELÉCTRICO
POR: TOMÁS BENJAMÍN NÚÑEZ GONZÁLEZ
FECHA: 2022
PROF. GUÍA: CESAR AZURDIA MEZA
PROF. CO-GUÍA: SANDRA CÉSPEDES UMAÑA

MODELAMIENTO DE CANAL PARA DESPLIEGUES DE IOT UTILIZANDO NANOSATÉLITES LEO

El encontrar un modelo de canal adecuado para los enlaces satelitales es uno de varios desafíos abiertos en las aplicaciones de *Direct-to-Satellite IoT* (DtS-IoT) servidas por nanosatélites *Low Earth Orbit* (LEO). Si bien se han propuesto varios modelos de canales satelitales, no existe una respuesta definitiva sobre cuál es más adecuado para representar el escenario estudiado.

En este trabajo se presenta un enfoque metódico para analizar, evaluar y comparar un conjunto de modelos de canal identificados como candidatos para representar el enlace a nanosatélites LEO en aplicaciones DtS-IoT. La metodología propuesta se compone de tres pasos: análisis cualitativo, simulaciones computacionales y una evaluación de desempeño en una configuración *Hardware-in-the-Loop*. El alcance de esta tesis abarca las dos primeras etapas descritas.

Los resultados obtenidos posicionan a los modelos de Akturan, Patzold y FSMC-TS como preseleccionados para su posterior análisis. Estos presentan el mejor *tradeoff* entre la representación de los fenómenos físicos, la rápida variación temporal del canal y complejidad computacional.

Adicionalmente, se propone un nuevo modelo, denominado Enhanced FSMC-TS, el cual corrige la ausencia de shadowing en el FSMC-TS. Al incorporar shadowing se logra una representación más precisa del escenario estudiado, dada la prevalencia de dicho fenómeno en éste.

RESUMEN DE LA TESIS PARA OPTAR AL GRADO DE
MAGISTER EN CIENCIAS DE LA INGENIERÍA,
MENCIÓN ELÉCTRICA
Y MEMORIA PARA OPTAR AL TÍTULO DE
INGENIERO CIVIL ELÉCTRICO
POR: TOMÁS BENJAMÍN NÚÑEZ GONZÁLEZ
FECHA: 2022
PROF. GUÍA: CESAR AZURDIA MEZA
PROF. CO-GUÍA: SANDRA CÉSPEDES UMAÑA

CHANNEL MODELING IN IOT DEPLOYMENTS SUPPORTED BY LEO NANOSATELLITES

The matter of finding an appropriate model for satellite links is still mostly unaddressed in Direct-to-Satellite IoT (DtS-IoT) applications served by LEO nanosatellites. While various channel models have been proposed for Land-mobile Satellite Systems, there is no definitive answer as to which one is most suited to represent the specific scenario under study.

In this work, we present a methodical approach to analyze, evaluate and compare a set of channels that have been identified as candidates to model the direct link to LEO nanosatellites in DtS-IoT applications. The proposed framework is a three-step approach consisting of comparative qualitative analysis, computer simulations and performance evaluation in a more realistic Hardware-in-the-Loop setting. The scope of this thesis encompasses the first two steps of the methodology.

The results presented position the Akturan, Patzold and Salamanca channels as pre-selected models for further analysis. These models present the best compromise between accurate representation of physical phenomena, accounting for time-variance and computational complexity.

Additionally, a novel approach, improving upon Salamanca's FSMC-TS proposal, is presented in this thesis. By introducing shadowing in the probability density funcion of the Bad (B) sector, the Enhanced FSMC-TS addresses one of the biggest limitations of the original FSMC-TS channel model.

"You should enjoy the little detours to the fullest.
Because that's where you'll find things
more important than what you want"
Ging Freecss

Acknowledgements

Con la adrenalina por los cielos al terminar este trabajo, comienzo a escribir esta sección donde debo reconocer y agradecer a todas las personas que me acompañaron durante esta larga etapa. Pensando que estaría dejando la parte más fácil para el final, me doy cuenta que, efectivamente, "otra cosa es con guitarra".

Comenzando por mi mamá, mis hermanos Clemente y Margarita, mi Tata y Bubu, mi papá, a la Tamy, al Álvaro, a la Paty y a los primos Gonzalez Bustos Asociados; muchas gracias por todo su apoyo, por aguantar los ratos de mal genio, y celebrar conmigo los momentos de alegría. Pero, por sobre todas las cosas, muchas gracias por permitir que me diera el lujo de enfocarme 100% en mis estudios, sin tener que preocuparme de nada más.

Agradezco también a Valeria, mi *partner* de más de 3 años ya, con notables papeles en esta historia como: compañera sibarita amante del sushi, compañera de ver animés, compañera de estrés por la U, entre otros. Gracias por la motivación constante, por el cariño y la preocupación.

Cómo olvidar al profesor César Azurdia y la profesora Sandra Céspedes, para quienes no tengo más que agradecerles por su buena voluntad y disposición para orientar y ayudarme en mi pasada por el DIE. No tengo problema en admitir que sin su apoyo, este trabajo seguiría siendo una hoja en blanco.

Por último, pero no por ello menos importante, agradezco también a mis amigos:

A Colvin; por las salidas a ver UFC, las noches de Smite, los intentos fallidos de sacarme a hacer deporte y un largo, largo etc. Gracias por ser de las pocas constantes en este torbellino de cambios.

A Pablo, Sven, Pipe y todos los Casuales de la 2; por los Quintay, los Algarrobo, los casa Pipe y un largo, largo etc. Gracias por la compañía en todas las ñoñerías, el cariño y la preocupación. Son realmente un 7.

A Claudio, Nico, Guauf y mis amigos y amigas de Eléctrica; Gracias por los almuerzos en los pastos, las tardes de estudio, las juntas de viernes por la tarde y un largo, largo etc. Ustedes han reafirmado la importancia de tener más cosas en la vida además del estudio o el trabajo.

A todos ustedes, muchísimas, muchísimas gracias.

Table of Content

List of Tables

List of Figures

Acronyms

5G NR	5G New Radio
AoI	Age of Information
BER	Bit Error Rate
BSC	Binary Symmetric Channel
CDF	Cumulative Distribution Function
CRDSA	Contention Resolution Diversity Slotted Aloha
CoAP	Constrained Application Protocol
CSI	Channel State Information
DtS-IoT	Direct-to-Satellite IoT
FSMC	Finite State Markov Chain
FSMC-TS	Finite State Markov Chain - Two-Sectors
GEO	High Earth and Geostationary Earth Orbit
HARQ	Hybrid Automatic Repeat Request
HITL	Hardware-in-the-Loop
IoST	Internet of Space Things
IoT	Internet of Things
IR-HARQ	Incremental Redundancy HARQ
LCR	Level Crossing Rate
LEO	Low Earth Orbit
LMS	Land Mobile Satellite

LOS	Line-of-Sight
LPWA	Low Power Wide Area
MAC	Medium Access Control
MEO	Medium Earth Orbit
MIMO	Multiple-Input Multiple-Output
NB-IoT	Narrowband IoT
NFV	Network Function Virtualization
NLOS	Non-Line-of-Sight
NOMA	Non-Orthogonal Multiple Access
NoMaGFA	Non-orthogonal Massive Grant-free Access
PDF	Probability Density Function
PSD	Power Spectral Density
RF	Radio Frequency
RTT	Round Trip Time
SA	Slotted Aloha
SDN	Software Defined Networking
SDR	Software Defined Radio
STAN	Simultaneous Tracking and Navigation
TFRC	TCP-Friendly Rate Control
WSS	Wide-Sense Stationary

Chapter 1

Introduction

1.1 Motivation

The framework of Internet of Things (IoT) was introduced initially by Kevin Ashton, and conceptualized as the convergence of telecommunications and information technology with different areas of the industry, such as home and building automation, logistics, electricity generation, among others [1]. The rapid growth and increasing interest in the IoT networking paradigm is a testament to the potential benefits this novel technology can provide to society, as seen by the wide variety of novel use cases enabled, both for the industry as well as in the end-consumer market [2]. Some examples of these applications are connected cars, smart homes, monitoring of manufacture equipment and e-Health.

Although the main idea behind IoT remains the same, substantial research has been carried out to improve and evolve the framework towards new directions. The Internet of Space Things (IoST) framework proposed in [1], is an example of this, aiming to reach truly ubiquitous global coverage for IoT deployments, through satellite-based data networks. This novel paradigm opens the door to a wide array of IoT usage scenarios, in which terrestrial links are unfeasible. Some examples that will profit from IoST connectivity are fauna tracking, monitoring of water resources, irrigation control in agriculture, and communications in disaster scenarios [1].

The usage of low Earth orbit (LEO) nanosatellites to serve terrestrial devices through Direct-to-Satellite links seems particularly promising, as it presents a viable, low-cost method of achieving global coverage, as presented in a study of LEO nanosatellites for 5G and beyond 5G applications [3]. However, various challenges arise when considering this context, specifically in the physical and Medium Access Control (MAC) layers [4]. Issues such as high IoT device density, the large impact of the Doppler Effect, the already mentioned constraints in energy and computational capability and a highly dynamic channel due to the satellites' mobility, need to be taken into account when designing the protocols and architectures to support this highly complex but promising paradigm.

In the realm of channel modeling, several approaches have been proposed to represent earth-to-satellite links [5–11]. Each model presents its own set of capabilities and constraints,

owing to the incorporation of different physical phenomena and the mathematical tools employed. The topic of channel modeling has been covered in various satellite communications surveys, both in the context of general Land-mobile Satellite scenarios [12], as well as specifically for CubeSat deployments [13], however, the analysis presented is almost exclusively descriptive. That is, there is little information available in literature pertaining to comparative analyses of different channel models, and how they manage to represent a specific scenario.

1.2 Problem Statement

As outlined previously, a formalization of space-based IoT is presented in [1], where the concept of *Internet of Space Things* based on CubeSats deployed in Low Earth Orbits is introduced. A practical realization of the system architecture proposed by the authors is presented, where a Direct Access Segment is explicitly identified. Figure 1.1 highlights said segment, along with the respective Direct-to-Satellite Channel associated with these types of links between terrestrial and satellite nodes.

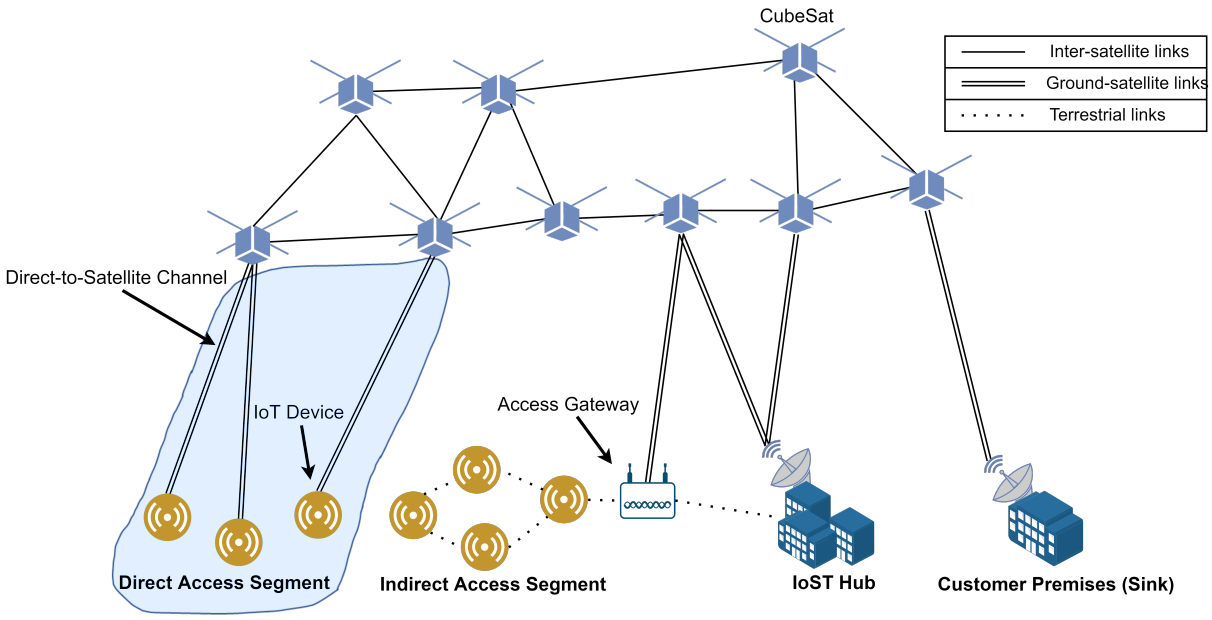

Figure 1.1: IoST framework architecture and direct-to-satellite links, adapted and simplified from [1].

Similarly, a thorough survey of the state of the art in Direct-to-Satellite IoT (DtS-IoT) is presented in [4]. The presented work is focused mainly on the physical and MAC layer, while still venturing into discussions about the upper communication layers. However, the challenge of physical channel modeling in the presented scenario is not addressed.

Conversely, Saeed et al. do cover the topic of channel modeling in CubeSat usage scenarios extensively in [13]. Various statistical approaches to channel models are presented and described in extensive detail, but they are evaluated only independently. That is, no comparisons are made between different models nor conclusions are drawn with respect to which approaches are better suited for specific scenarios.

There is a noticeable gap in the DtS-IoT framework, since there is no clear answer as to what might be the most suited channel model to represent the physical links between terrestrial and satellite nodes in LEO. Consequently, the challenge of evaluating, comparing and selecting appropriate channel models for Direct-to-LEO Satellites is tackled in this work.

1.3 Hypothesis

- A channel model that incorporates the Doppler Effect, multipath, shadowing and a high-degree of time-variance can accurately capture the physical link dynamic of the Direct-to-LEO Satellite IoT scenario.

1.4 Objectives

The objectives of the work are summarized as follows:

- **General objective:** To evaluate, select, validate and enhance a proper channel model to employ for the Direct-to-LEO Satellite IoT scenario, by using a methodical and systematic approach.
- **Specific objectives:**
  - To analyze existing channel model proposals that are aplicable to the Direct-to-LEO Satellite IoT communications scenario.
  - To define a methodical framework to be employed for the assessment, comparison and evaluation of channel models for LEO satellite communication systems, based on how accurately they represent the scenario under study and its inherent challenges.
  - To evaluate and analyze the impact of channel models in LEO satellite communications systems theoretically and via simulations, utilizing BER as the key performance metric.
  - To propose and evaluate enhancements to existing channel models, to better represent the effect of shadowing in the Direct-to-LEO Satellite IoT scenarios.

1.5 Thesis Structure

The remainder of this thesis is structured as follows: In Chapter 2, a general-to-specific overview of Satellite Communications, LEO Satellites, Nanosatellites in Satellite Communications and Satellite IoT is presented, along with challenges relevant to channel modeling in the studied scenario. Following that, Chapter 3 provides a detailed description of channel modeling in Satellite environments, including relevant physical phenomena and extensive descriptions of existing channel models found in literature. In Chapter 4, a three-step framework to comparatively analyze channel models is presented, including an analysis of initial results obtained. Subsequently, Chapter 5 introduces a novel channel model proposal, con-

structed as an improvement on a model evaluated in the previous chapter, addressing its biggest limitation. Finally, Chapter 6 presents a set of conclusions drawn from this work, in addition to describing potential directions for future work.

Chapter 2

Background

In this chapter, a review of the state of the art is presented, initially covering satellite communications and its evolution to what is known today. Following that, we take a deeper look into LEO Satellite applications specifically. Subsequently, the topic of Nanosatellite Communication Systems is covered in greater detail. Afterward, the subject of challenges and applications of Satellite-based IoT is presented. Finally, the literature review is summed up in the final section of this chapter, where the challenges relevant to channel modeling of the DtS-IoT scenario served by LEO nanosatellites are discussed.

2.1 Satellite Communications

The field of Satellite communications has evolved and grown to the point of becoming an essential component in communication technologies. Some examples of these applications range from traditional, well-known ones like positioning systems and satellite television, to newer developments such as internet backhaul and coverage extension to remote areas [14–16]. Furthermore, renewed interest in the field and a high degree of private investment are driving forward the development of more and more novel use cases for satellite communication systems. 5G non-terrestrial networks and space communications serve as prime examples of this [17].

In [14], the widespread usage of satellites in communication systems is explained by addressing many of their inherent advantages. Elbert highlights how most of the benefits of satellites in communication environments stem from the basic physics behind these systems, most importantly from the fact that a single satellite can provide substantial ground coverage. Flexible wide area coverage varying with orbit height, mobile/wireless communication independent of location, and fast construction and deployment of new terrestrial sites at a low cost are some examples of said benefits [14].

Traditional satellite communication systems can be characterized by the parameters of its two main segments and how they interact with each other, the earth segment and the space segment [14]. Some examples of defining aspects of satellite communication systems include whether ground stations are mobile or stationary in the earth segment, the frequency

band employed for the Radio Frequency (RF) links, as well as constellation size and type. Directly related with the latter, orbital height of the space segment is one of the most common characteristics utilized to classify satellite systems. Although there is no formal consensus in the scientific community, one of the most common categorizations is composed of Low Earth Orbit (LEO), Medium Earth Orbit (MEO) and High Earth and Geostationary Earth Orbit (GEO).

NASA sets each categories orbital heights as follows [18]: LEO comprises orbits ranging from 180 to 2000 [km]. MEO can be considered as anything between LEO and the Geostationary orbit, from 2000 to 35780 [km]. Despite this, most common orbits are located around 20200 [km]. Finally, GEO can be considered to be anything above 35780 [km], with this specific orbital height consisting of the geosynchronous orbit.

Despite the unavoidable reduced coverage footprint at lower orbital heights, LEO satellites possess a series of advantages that make them very appealing for commercial communication systems. Small roundtrip times, path loss and overall costs are some of the benefits of using LEO satellites, as opposed to MEO or GEO alternatives [19]. Said benefits prove to be particularly relevant for IoT deployments, in which total cost and transmission power are the main constraints, with delay also proving to be a key variable for specific delay-sensitive applications. Section 2.2 explores different aspects of LEO Satellite communication systems in more detail.

2.2 LEO Satellite Communications

LEO satellites are undoubtedly becoming more and more prominent every day in modern communication systems. Their main comparative advantages include a low-cost solution to providing global coverage, even to remote or underdeveloped regions of the globe. Furthermore, this is accomplished with significantly lower delays, when compared to their Geostationary counterparts [4,16,19,20]. However, in spite of the growing interest in this technology from both academia and the industry, there are various challenges associated with it, most notably in commercial deployments of LEO constellations.

Ventures such as Iridium and Globalstar demonstrated that the production and deployment costs of LEO constellations were for some time more expensive than it was initially assessed, with both projects going into bankrupcy in 1999 and 2002 respectively [16, 20]. Nevertheless, extensive research and technological advancements, as well as continuous investments in the private sector, have allowed several LEO satellite systems to continue operating, including the recovery of Iridium and Globalstar. The former remains focused around satellite phone coverage, while the latter has expanded their focus to target key market segments such as government & public safety, asset tracking and recreational users [16].

Today, the growing interest in global broadband Internet access has allowed systems such as OneWeb and SpaceX's Starlink constellation to grow rapidly. These projects serve as prime examples that LEO satellites could potentially solve the problem of ubiquitous Internet access, at a feasible cost [16, 20]. Similarly, as discussed in [17] and [21], the potential of satellite communications in 5G enablement is unquestionable, with LEO constellations playing a pivotal role.

Current research in LEO Satellite Communications is varied, ranging from attempting to define potential system architectures and potential novel use cases, to overcoming some of the inherent challenges associated with a lower orbital height. In [3], the topic of small satellite LEO constellations for 5G systems is studied, proposing a Walker star constellation architecture. Complementing the theoretical work presented, a performance analysis of both Ground-to-Satellite and Inter-Satellite links is presented as well. Similarly, a thorough architectural analysis of LEO satellite constellations for IoT scenarios is presented in [22]. This work is focused mainly on constellation design with or without Inter-Satellite Links, the effect of interference in a potential communications system, and the compatibility for interoperation with terrestrial IoT deployments. In a similar vein, an overview of architectural considerations for broadband LEO communication systems is shown in [19]. In this work, the key topics covered correspond to the advantages and disadvantages of using Walker Delta or Walker Star constellations, viable inter-satellite switching schemes, coverage schemes and interference coordination between LEO and GEO satellite systems.

Regarding novel applications, the topic of navigation employing LEO satellites has been explored in-depth by Kassas and Khalife in various works. In [23], a framework employing an Extended Kalman Filter to estimate a receiver's position based on the Doppler effect is proposed, obtaining an accuracy of up to 11 $[m]$ with a 25-satellite constellation through simulations. This work is later expanded upon in [24], formalizing their framework now labeled Simultaneous Tracking and Navigation (STAN). Finally, in [25], experimental results utilizing Starlink's LEO satellite signals are introduced, achieving a horizontal position error as small as 7.7 [m].

Cooperative schemes have also been a topic of interest in the scientific community, to tackle some of the common challenges of communication systems in LEO satellite scenarios. For example, a novel routing protocol labeled *Network Coding based Multipath Cooperative routing* is presented in [26], with a focus on data transmission efficiency and reducing the complexity of the system. This novel protocol accounts for the long link delay that characterizes satellite topologies and is cooperative in nature, delivering different parts of data in a dynamic fashion. Conversely, at the MAC layer, the problem of random access is tackled in [27] using a cooperative strategy to adapt traditional random access protols like Aloha, Slotted Aloha (SA) and Contention Resolution Diversity Slotted Aloha (CRDSA). Significant improvements with respect to throughput, stability and energy efficiency are achieved, when comparing the access protocols with their non-collaborative equivalents.

At the physical layer, in [28], the challenge of performing timing and frequency synchronization for downlink transmissions of 5G New Radio (5G NR) signals over LEO satellites is explored, affected by inherently large Doppler shifts. Conversely, different variants of Chirp Spread Spectrum-type modulations are explored in [29], aiming to determine the viability of these techniques for LEO satellite IoT deployments. In [30], the applicability of Masive Multiple-Input Multiple-Output (MIMO) techniques commonly employed in terrestrial communication systems is studied in the context of systems based on LEO constellations, demonstrating that the proposed Massive MIMO system with Fractional Frequency Reuse produces significant improvements in performance.

The topic of channel modeling in LEO satellite environments has been a topic of substan-

tial research as well. The effect of rain attenuation in LEO satellite systems operating at 10 [GHz] and above is studied in [31], proposing a stochastic dynamic model to capture the impact on the communication link. This model is constructed as an extension of the well-known Maseng-Bakken model for fixed satellite communication links. Furthermore, in [32] and [33], the effects of ionospheric scintillation in LEO satellite communication systems are explored, with the latter focusing specifically on systems employing LoRa at the physical layer. Finally, an FSMC channel state model is proposed in [34], providing a time-correlated method to estimate in a more realistic manner whether the channel is in a Line-of-Sight (LOS) or Non-Line-of-Sight (NLOS) state. This work is of particular interest, as the dynamic model, generated via novel ray tracing simulations, is compared against a publicly available model from the 3GPP.

Evidently, most of the physical layer related work is centered around overcoming some of the inherent limitations of low orbital heights. A large Doppler Shift, non-stationary orbits with time-varying trajectories, a relatively small coverage footprint, highly dynamic channels with a variety of physical phenomena and large distances requiring Low Power Wide Area (LPWA) technologies are some of issues that must be considered for the physical layer. Section 2.5 provides an in-depth view of how these and other challenges of the scenario must be accounted for to determine what constitutes an appropriate channel model.

Lastly, nanosatellites, satellites that are characterized by their extremely small size, are of particular interest in literature as well. By minimizing cost, size and energy consumption, nanosatellites have been key enablers of LEO satellite communication systems. However, due to the critical importance of this subject, the literature on nanosatellites is covered separately in the following section.

2.3 Nanosatellites in satellite communications

Nanosatellites, or more generaly speaking, small LEO satellites, are characterized by their significantly lower cost, communication latency and energy consumption, as well as high fault tolerance [35]. Bringing down the production and launch cost to numbers as low as 100.000 to 200.000 USD, nanosatellites have allowed the space industry to grow considerably, offering new applications such as space observation, earth observation and telecommunications [13, 35]. Consequently, substantial research has been conducted to explore the different aspects of nanosatellite communications, including the discussion of potential applications enabled by these new platforms, as well as attempting to address some of the challenges stemming from their limitations.

A survey of potential system architectures, physical structure and components, protocols, as well as future challenges for small satellites and Cubesats, is presented in [35]. The review presented is extensive, covering a wide variety of subjects, including the matter of channel modeling. Protocol selection at the physical and upper layers, routing and security are presented as some of the more relevant challenges. While the inherent design limitations of the smaller platform are described as severe, the authors state that the miniaturization of hardware components should still allow compliant operation of small satellite communication systems without major issues.

Concerning more specific, in-depth assessments, an extensive review and evaluation of MAC protocols for Satellite IoT nanosatellite systems is presented in [36]. Well-known protocols are analyzed through the lens of a nanosatellite IoT system, including Aloha-based protocols, Reservation-based and Adaptive protocols, Interference Cancellation-based protocols as well as hybrid approaches. These protocols are evaluated and compared using both quantitative metrics such as the normalized offered load, normalized throughput and packet loss ratio, as well as qualitative metrics such as the energy efficiency, complexity of implementation and topology impact.

A similar work centered exclusively around CubeSats is shown in [13]. In addition to providing a very thorough review of CubeSat missions and a comparison of the manuscript with related surveys, the analysis presented in the manuscript is structured around the different layers of the TCP/IP model. The key subjects covered include constellation design, channel modeling, link budget, modulation and coding, MAC protocols, routing protocols and application layer elements. The Channel Modeling section of this work is of special interest, due to the great number of proposals that are listed and described in detail.

Similarly, the degree to which LoRa exhibits immunity to the Doppler Effect in CubeSat communications is assessed in [37]. The focus on LoRa specifically stems from the great promise shown by this modulation technology, given the scarcity of power and long distances required to cover in the scenario under study. The authors empirically measure the impact of the Doppler effect in LoRa signals, both in an indoor laboratory setting, as well as in a more realistic, outdoors environment. The experimental results presented illustrate that for Spreading Factor $SF \leq 11$, there is a significant margin of immunity to both dynamic and static Doppler effects, down to orbital heights as low as 200 [km]. It is worth noting, however, that these conclusions are applicable only to scenarios with relatively isolated Doppler effects, that is, in the absence of multipath. The authors justify this limitation by suggesting that satellite LoRa communications are unaffected by multipath, but no evidence is provided to support this claim in [37].

Another relevant work related to CubeSats is presented by Akyildiz and Kak in [1], where the concept of Internet of Space Things/CubeSats (IoST) is introduced. As the name suggests, this paper is focused specifically around proposing a novel framework for IoT applications supported by CubeSats, leveraging Software Defined Networking (SDN) and Network Function Virtualization (NFV) as core elements to control hardware and simplify network management. Use Cases for IoST and System Architecture are the main topics covered in the manuscript. The latter is composed mainly of 4 layers: the Infrastructure Layer, the Control and Management Layer, the Policy and Orchestration Layer, and finally, the Security and Privacy Sublayer. The Access Network architecture proposed as part of the Infrastructure layer is of particular interest, acknowledging the existence of a Direct Access segment. This segment is composed of sensing devices that establish direct communication links with CubeSats.

In a similar vein, this idea of a Direct Access segment is further explored in [4], studying what is labeled as the *Direct-to-Satellite IoT* architecture. The topics reviewed include existing satellite protocols and LPWA technologies, potential applications or revisions of said protocols to accomodate DtS-IoT scenarios and challenges to consider for DtS-IoT satellite

constellations. Similarly to what was stated in [37], LoRa is considered to be a very appealing modulation technology to employ for these scenarios, due to the exceptional link budget achieved, with very little power required, while retaining a great degree of robustness to signal degradation. It is worth noting, however, that the topic of channel modeling is not covered in this work.

The literature review for nanosatellites and CubeSats illustrates that there is definitely great potential in these smaller, significantly less expensive satellite platforms. IoT in particular appears to be a very appealing field of application for satellite-based communication systems. The following section presents further research concerning Satellite-based IoT systems.

2.4 Satellite-based IoT

The previously referenced works in [4] and [1] provide an excellent overview of the Satellite IoT paradigm. In this section, additional literature is presented, to illustrate the different aspects of this new architecture that are being studied with greater depth, including some of the new challenges faced, as well as potentially novel applications enabled by this framework.

Concerning multiple access, a novel non-orthogonal access protocol is proposed in [38], denominated Non-orthogonal Massive Grant-free Access (NoMaGFA). This approach reaps the benefits of both traditional Non-Orthogonal Multiple Access (NOMA) and Resource Allocation-based technologies, and allows a significant performance improvement in asynchronous satellite-based IoT transmissions, from the viewpoint of system throughput and robustness. Additionally, as mentioned throughout the manuscript, the system has been designed from the ground up with 6G in mind, aiming to satisfy the strict network requirements with respect to coverage and robustness.

Similarly, the task of designing an optimal error control method at the data link layer for Satellite IoT is tackled in [39]. Both simple Hybrid-Automatic Repeat Request (HARQ) and Incremental Redundancy HARQ (IR-HARQ) are studied using the Age of Information (AoI) metric for optimization, subject to reliability constraints. Analytical, closed-form expressions for the AoI are derived for both retransmission schemes, with simulation results presented as well to complement these theoretical results. It is concluded that below a given propagation delay threshold, the IR-HARQ can provide a considerable benefit with respect to the AoI metric employed.

At the application layer, the topic of proper application protocol selection has received some attention. In [40], and later again in [41], Bacco et al. compare the two most widely employed application layer protocols for IoT applications in the context of space-based IoT networks, MQTT and Constrained Application Protocol (CoAP). These protocols are compared using various metrics, such as Energy efficiency, protocol overhead and reliability, in addition to goodput in relation to normalized load to measure performance. It is concluded that CoAP is a more attractive choice than MQTT, mainly due to the greater performance achieved by the former in conjunction with a TCP-Friendly Rate Control-based (TFRC) congestion control. Additionally, CoAP is mentioned to possess greater overall flexibility, when compared to MQTT.

Concerning applications, various new directions are being currently explored. In the edge computing and machine learning domains, a Satellite IoT Edge Computing architecture is presented in [42]. Conceived to deal with the massive influx of data that is generated by IoT sensor networks, this architecture aims to significantly increase the speed with which data is processed, by leveraging edge computing and deep-learning technology. Simulation results performed with a 66 satellite Walker constellation demonstrated that several complex neural networks could be successfully trained using a distributed computing approach. For inference, results for both single node as well as distributed computing methods are presented, with reasonable inference times achieved in both scenarios.

Due to the mission-critical nature of various defense applications, requiring ubiquitous coverage and a rapid response time, satellite-based IoT can prove to be a very appealing solution in military applications as studied in [43]. Some of the examples provided include support for search and rescue missions during disaster scenarios, border intrusion detection to identify terrorist movement, illegal migration and drug trafficking, in addition to airspace protection, allowing accurate navigation even under poor visibility conditions. Additionally, the authors propose Narrowband IoT (NB-IoT) as the LPWA techonology to be used for satellite IoT, mainly due to the green nature of the technology, as well as due to its reliability allowing continuous operation over the course of several years.

Satellite IoT Applications in rural environments have been also thoroughly studied, with the potential for ubiquitous coverage as one of its most attractive features. An integrated 5G and IoT use case for the environmental monitoring of large rural areas for agriculture is presented in [44], utilizing a hybrid non-terrestrial segment comprised of drones and satellites. Drones collect and aggregate data from terrestrial sensors to detect fire alarms, delivering messages through a satellite uplink to a control center. The initial analytical results presented show promise, and encourage further study to optimize and/or simulate the proposed system.

Evidently, there is great potential for IoT applications utilizing the ubiquitous, low cost and energy efficient coverage provided by satellites. Nevertheless, there are still a variety of challenges to address in these types of deployments, as it has been seen in the works reviewed so far. Specifically, the matter of channel modeling for IoT applications supported by Direct-to-LEO nanosatellites or CubeSats, is still an open question. Despite being discussed sporadically in surveys and reviews, there is no clear-cut answer as of yet.

2.5 Channel modeling challenges in the scenario under study

The main objective of this section is to bring together all the challenges and limitations presented up to this point of the DtS-IoT scenario. These challenges need to be considered when designing the architectures and protocols that will be employed to support IoT deployments through Direct-to-LEO nanosatellite links. In this section, we discuss the challenges that are most relevant to the definiton of a proper channel model. Figure 2.1 is presented as a reminder of the topology under study.

Satellite links usually imply relatively high delays, mainly due to the large distance that

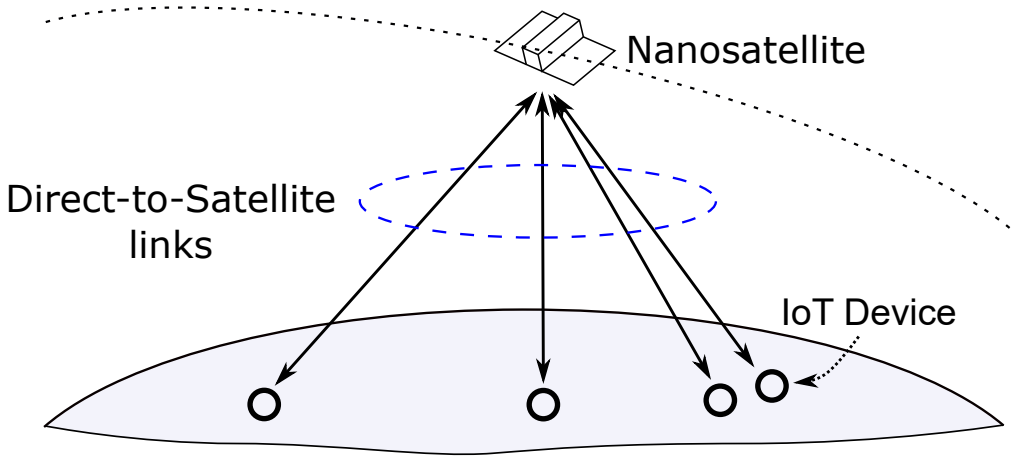

Figure 2.1: Illustration of a Direct-to-Satellite IoT deployment. Devices establish a bidirectional link to a low Earth orbit nanosatellite, as there is no terrestrial gateway station. Each IoT device observes a potentially different satellite elevation angle.

separates the endpoints. Although not as significant as with Geostationary satellites, as LEO orbit heights span from 200 to 2000 [km], the Round Trip Time (RTT) can still be as high as 10 [ms]. In [45], the system performance degradation due to delayed Channel State Information (CSI) caused by different values of RTT, including those associated with LEO orbits, is studied. For an RTT value of 10 [ms], the harmful effect of delayed CSI increases rapidly with user speeds, with a noticeable impact at 20 [km/h] and above. It is worth mentioning that the channels evaluated consist of the Loo, Lutz and Nakagami fading models.

Energy efficiency is key for IoT deployments, with battery life expectancies for land-based nodes reaching as high as 10 years [46]. In most cases, abundant electrical power is not readily available at the terrestrial nodes. Although this limitation is a known factor for common IoT scenarios, the use of LEO nanosatellites to establish direct links imposes an additional power restriction on the satellites used as gateways for the IoT devices. This narrows down physical layer options to long-range LPWA technologies, such as LoRa, NB-IoT, SigFox or even 5G [4, 44]. Additionally, the scarcity of available transmission power usually means that a strong line of sight is needed, making it very challenging to establish communication links at low elevation angles [13].

Directly related to power scarcity, the lack of on-board processing capacity both in land-based nodes, as well as in the nanosatellites, severely limits the complexity of the communication protocols and technical solutions available [47, 48]. This may have a large impact in the applicability of complex yet useful mechanisms such as channel estimation [13].

On the other hand, due to the very high relative velocity between terrestrial nodes and LEO satellites, the Doppler effect must be taken into account in the direct link [49]. With speeds of up to 8 km/s, the relative Doppler shift (δF) can be as high as 25 ppm [37]. In addition to this, the highly dynamic nature of said Doppler shift, measured through its derivative ($\delta F'$), must also be considered. Although some physical layer technologies tend to show a certain degree of immunity to this effect [37], it is a phenomenon that should be

contemplated when selecting a channel model.

In most situations, orbits with a high inclination must be utilized to achieve global coverage with LEO constellations [50]. In conjunction with the Earth's intrinsic movement, the relative trajectories of satellites with respect to the Earth's surface change over time, resulting in non-stationary link parameters between land-nodes and satellites [51]. Consequently, channel models should be dynamic enough to account for communication windows of variable length and maximum elevation angle at different points in time.

As outlined previously, LPWA technologies appear among the most attractive physical layer options for the Earth-to-Satellite links. These technologies are characterized by their long range, low power consumption and robustness to channel degradation, in addition to their very limited bit transmission rates. Although not extensively tested in the LEO satellite environment, the research with LoRa presented in [36, 37, 52, 53] shows the potential value of this solution, making it one of the more attractive LPWA physical layer technologies to utilize. Conversely, a case can also be made for NB-IoT as a potential technology, owing to its green nature and great reliability when operating for several years, as remarked in [43]. Other works defending NB-IoT and variants of it for usage in Satellite IoT can be found in [54–56]. Although there is no consensus as to which LPWA technology should be utilized, the literature demonstrates that the physical layer should indeed be restricted to these types of technologies.

The usage of LPWA modulations for the physical layer imposes an additional challenge to consider for the scenario. The presence of large Doppler spread due to the high relative speed between satellites and ground nodes, leads to a very small coherence time associated with the satellite channel. This phenomenon, in conjunction with the low bitrate associated with LPWA technologies, causes the channel to be perceived as highly dynamic, with more than one channel realization observed during the transmission of one symbol [57, 58]. As such, degradation is caused not only by slow fading, but fast fading as well.

The challenges described in this section include only those effects that are considered to be relevant for the selection of an appropriate channel model. Characteristics of the scenario affecting other aspects of the communication system are out of the scope of this work. An example of this is the high device density requirement, that despite having a large impact in interference modeling and random access schemes, is not pertinent to the task at hand. Channel modeling as a whole is an extensive topic, and will be covered separately in chapter 3.

Chapter 3

Channel Modeling in Satellite Environments

In this chapter, we review the fundamentals of Channel Modeling in wireless communication systems. The topic is initially covered from a general standpoint, later focusing on LEO satellite communications, in the context of potential DtS-IoT applications.

3.1 Fundamentals of Channel Modeling

Communication channels are defined by Proakis and Salehi as the physical medium that is utilized to send the signal from transmitter to receiver [59]. Depending on the specific application, the medium can range from wire lines and optical fibers, to free space itself. All channels introduce some degree of random signal degradation, causing the signal at the receiver end to be distorted, when compared to the originally transmitted signal.

There are a wide variety of factors that can contribute to signal degradation in the physical channel. Additive noise is one of the most prevalent effects, usually occuring due to thermal noise in electrical components, but also being caused by external elements, such as other users occupying the channel at the same time. Other effects that contribute to signal degradation include signal attenuation, phase and amplitude distortion, and multipath distortion [59].

The degree to which the different factors affect the communication system depends on the characteristics of the transmission medium. As Pätzold and Goldsmith remark in "Mobile Radio Channels" [60] and "Wireless Communications" [61] respectively, the fundamental physical phenomena that characterize wireless channels are a consequence of signal propagation and subsequent interactions with the medium itself. Pätzold identifies reflection, diffraction and scattering as these essential phenomena in wireless communication channels. However, multipath is then introduced as the observable effect at the received end caused by the previously described effects. Multipath occurs due to the superposition of multiple delayed and attenuated copies of the transmitted signal at the receiver end, originating from interactions with objects present in the environment, such as vehicles, buildings and trees. The differing amplitudes and phases of the superposed waves cause both destructive and

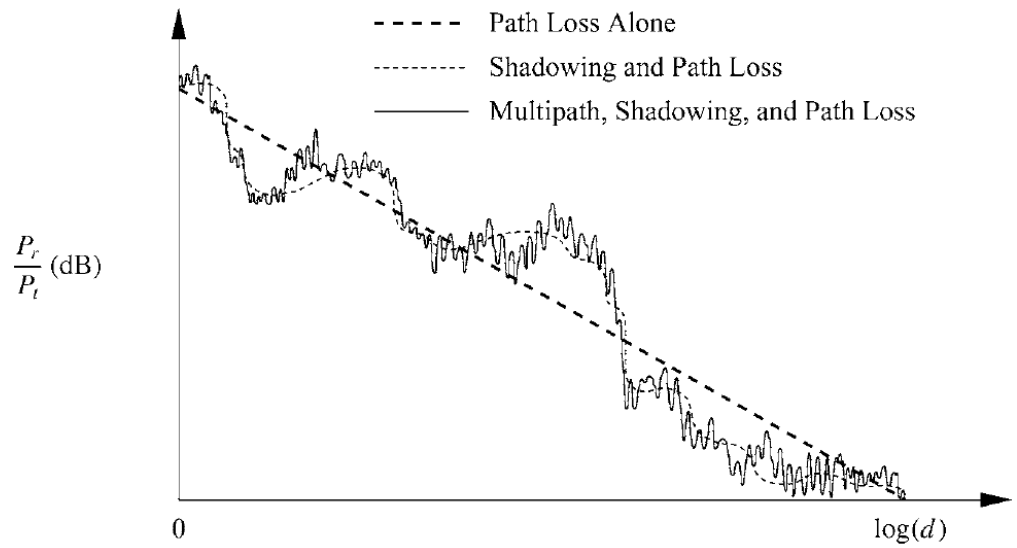

Figure 3.1: Effects of path loss, shadowing and multipath over distance. Extracted with Cabridge University Press' permission from "Wireless Communications" [61].

constructive interference at varying intervals, leading to distortion in the received signal.

Conversely, Goldsmith presents a different approach to identify the effects causing signal degradation in wireless radio environments, making a distinction between *large-scale fading* and *small-scale fading*. Path loss and shadowing are associated with large-scale fading, since variations in received power caused by these effects occur over large distances (around 10-1000 [m] for path loss, 10-100 [m] for shadowing). The former is caused by distance-based attenuation as well as other propagation effects of the channel, with path loss models usually assuming that the received signal power is static for a given transmitter-receiver distance. Shadowing, on the other hand, is attributed to obstacles found in the signal path that attenuate the received signal power through absorption, reflection, scattering, and diffraction. Since the effect of shadowing depends on the size, location and dielectric properties of the object, it is usually modeled stochastically in relation to distance. For small-scale fading, the most prevalent loss mechanism is multipath, due to how quickly power variations occur over very short distances. Multipath is mainly caused by the constructive and destructive addition of the transmitted signal after following multiple paths to reach the receiver. Once again, this effect is modeled stochastically. Figure 3.1 illustrates how the three effects described by Goldsmith, path loss, shadowing and multipath, are combined to cause varying degrees of signal degradation as the transmission distance increases.

Despite the minor differences in the approaches presented by Goldsmith and Pätzold, both include the Doppler effect as another relevant phenomena that can introduce distortion in wireless environments. The Doppler shift, is caused by relative motion between transmitter and receiver, leading to a perceived shift in the frequency of the received signal. Additionally, the frequency dispersion phenomena manifests in the time domain by making the Channel's impulse response time-variant [59]. The time-frequency domain analysis of how the Doppler effect contributes to signal distortion in wireless communications is analyzed extensively in [60] and [61].

Several different approaches to model wireless channels have been proposed over the last few decades. These range from well-known empirical path-loss models, like the one proposed by Hata for large urban macrocells [62], as well as geometrical approaches employing ray-tracing principles for multipath modeling [63]. However, as stated by Goldsmith, these types of approaches have significant limitations. On one hand, empirical path-loss exhibit decreasing accuracy as the application scenario differs from the original model conditions, while ray-tracing models, despite successfully capturing the multipath phenomena, are rarely applicable in practical applications.

Consequently, in most applications wireless channel models must be characterized statistically, typically through their time-varying impulse response. The task of channel modeling then can be reformulated as finding the appropriate statistical representation that captures the effect the previously mentioned physical phenomena present in the medium used for signal transmission.

3.2 Key Physical Phenomena in LEO Satellite Environments

As shown in the previous section, there is a general consensus with respect to the fundamental physical phenomena that are relevant for the statistical modeling of radio channels. For an IoT scenario supported by direct links to LEO satellites, multipath fading and shadowing are very prevalent effects [12, 13]. Additionally, direct-to-LEO satellite links are heavily affected by the Doppler effect, due to the extremely high tangential speeds required to maintain the devices in orbit (upwards of 7 [km/h]), as studied in [37, 49].

Consequently, the three key physical phenomena relevant to channel modeling are considered to be multipath, the Doppler effect and shadowing. In sections 3.2.1, 3.2.2 and 3.2.3, said effects are described in detail, focusing on their mathematical representation and their impact in overall signal quality.

3.2.1 Multipath

A very effective way to model multipath environments is described in figure 3.2, in which the phenomenon is represented by N local scatterers placed at different locations surrounding a mobile station communicating with a remote base station. The deduction presented follows Pätzold's mathematical description of multipath in [60].

If $x_{BB}(t)$ is considered to be the baseband representation of the transmitted signal, the corresponding bandpass signal $x_{BP}(t)$ is expressed as follows:

$$x_{BP}(t) = \mathrm{Re}\left[x_{BB}(t)\mathrm{e}^{j2\pi f_0 t}\right], \tag{3.1}$$

where f_0 represents the carrier frequency employed. The resulting bandpass multipath signal $y_{BP}(t)$ can be modeled as follows:

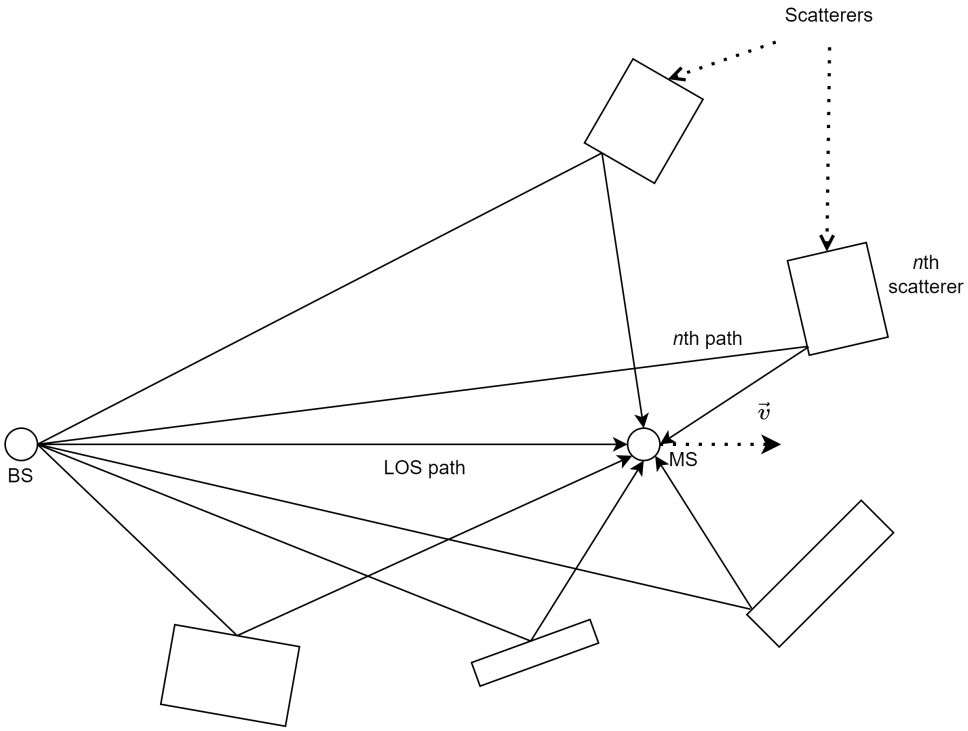

Figure 3.2: Multipath modeling with a mobile station, base station and local scatterers placed around the former. Adapted from [60].

$$y_{BP}(t) = \mathrm{Re}\left[\sum_{n=1}^{N(t)} c_n(t)\mathrm{e}^{j\phi_n(t)} x_{BB}\left(t-\tau_n^{'}(t)\right)\mathrm{e}^{j2\pi f_0(t-\tau_n^{'}(t))}\right], \tag{3.2}$$

where $c_n(t)$, $\phi_n(t)$ and $\tau_n^{'}(t)$ represent the attenuation, phase shift and delay asssociated with the path created by the nth scatterer, with $n = 1, 2, ..., N$. The receiver's relative movement causes each parameter to be potentially time-varying, as shown by the explicit dependence on t. For the sake of simplicity, during the mathematical derivation it is assumed that no Line of Sight component is present.

From the bandpass multipath signal representation $y_{BP}(t)$ presented in equation 3.2, the following expression for the baseband multipath representation $y_{BB}(t)$ is deduced:

$$y_{BB}(t) = \sum_{n=1}^{N(t)} c_n(t)\mathrm{e}^{j(\phi_n(t)-2\pi f_0\tau_n^{'}(t))} x_{BB}(t-\tau_n^{'}(t)). \tag{3.3}$$

Equation 3.3 illustrates how the resulting signal in a multipath environment can be interpreted as a superposition of attenuated, phase-shifted, delayed reflections of the transmitted signal, where the attenuation, phase and delay coefficients are time-varying. Furthermore, the input-output relationship between the baseband transmitted and received signals can be employed to deduce the channel's time-variant impulse response, as seen in equation 3.4.

$$h(\tau^{'},t)=\sum_{n=1}^{N(t)}c_n(t)\mathrm{e}^{j(\phi_n(t)-2\pi f_0\tau_n^{'}(t))}\delta(\tau^{'}-\tau_n^{'}(t))). \tag{3.4}$$

The high amount of variability in the channel parameters usually motivates a statistical treatment of the channel model. To simplify the analysis, equation 3.4 is restricted to be valid within a small window of time, for $t \in [t_0, t_0 + T_0]$, with t_0 being an arbitrary reference point in time and T_0 the duration of said window. If T_0 is sufficiently small, then the number of propagation paths $N(t)$, attenuation coefficients $c_n(t)$, phases $\phi_n(t)$, receiver speed $v(t)$ and angle-of-arrival of the n-th with respect to the mobile speed $\alpha_n(t)$ can considered to be static. Consequently, the dependence on t for these variables will be ommitted moving forward.

Furthermore, the propagation delays $\tau_n^{'}$ associated with each path can be expressed in terms of the Doppler shift and the propagation delay at reference time t_0. The Doppler effect will be explained in further detail in section 3.2.2, but it is essentially a frequency shift that is observed when there is relative motion between transmitter and receiver. Under the assumption that the mobile speed v is significantly smaller than the speed of light c_0, the resulting expression is obtained:

$$\tau_n^{'}(t)=\tau_n^{'}(t_0)-t\frac{v}{c_0}\cos(\alpha_n). \tag{3.5}$$

As seen in equation (1.2) of [60], it is possible to substitute $\frac{v}{c_0}=\frac{f_{\max}}{f_0}$ in the previous expression. It is worth noting that $f_{\max}$ denotes the maximum Doppler frequency, observed when the angle-of-arrival is zero. Similarly, by defining f_n as the nth path's Doppler frequency, with $f_n = f_{max}\cos(\alpha_n)$, the propagation delays can be expressed in the following compact form:

$$\tau_n^{'}(t)=\tau_n^{'}(t_0)-t\frac{f_n}{f_0}. \tag{3.6}$$

Substituing the expression from equation 3.6 in equation 3.4, and using the following approximation:

$$\delta(\tau^{'}-\tau_n^{'}(t_0)+t\frac{f_n}{f_0})\approx\delta(\tau^{'}-\tau_n^{'}(t_0)), \tag{3.7}$$

the following expression is obtained for the channel's impulse response:

$$h(\tau^{'},t)=\sum_{n=1}^{N}c_n\mathrm{e}^{j(2\pi f_n t+\phi_n-k_0D_n)}\delta(\tau^{'}-\tau_n^{'}). \tag{3.8}$$

The notation was simplified by replacing $\tau_n^{'}(t_0)$ with $\tau_n^{'}$, and using variables $k_0 = \frac{2\pi}{\lambda_0}$ and $D_n = c_0\tau_n^{'}$ to replace $2\pi f_0\tau_n^{'}$, as shown in the following equation:

$$2\pi f_0\tau_n^{'} = \frac{2\pi}{\lambda_0}c_0\tau_n^{'} = k_0 D_n. \tag{3.9}$$

It is worth noting that the final term in the phase coefficient, k_0D_n, changes rapidly even for small variations in total path distance, increasing by 2π whenever the total distance travelled D_n increases by multiples of λ_0. Using LoRa as an example, λ_0 can be as small as 30 [cm] for the commonly used 915 [MHz] band.

To proceed with the stochastic modeling of the channel, random variables are introduced to approximate the channel's behavior. Under the assumption that both ϕ_n and $\phi_n^{'} = k_0D_n$ are uniformly distributed in the $[0, 2\pi]$ interval, the variable $\theta_n = \phi_n - \phi_n^{'}$ follows the same distribution as well. Further simplifications can be made if the difference between propagation delays $\tau_{\mathrm{i}}^{'}$ is significantly smaller than the symbol duration T_{sym}, that is, if $|\tau_n^{'} - \tau_m^{'}| \ll T_{sym}$, for $m, n = 1, 2, ..., N$. In this special case, the propagation delays for each path $\tau_n^{'}$ can be estimated to be equal, that is $\tau_n^{'} \approx \tau_0^{'} \quad \forall n = 1, 2, ..., N$. By using this approximation and defining $\mu(t)$ as follows:

$$\mu(t) = \sum_{n=1}^{N} c_n \mathrm{e}^{j(2\pi f_n t + \theta_n)}, \tag{3.10}$$

a more compact form of the impulse response can be reached, as shown in equation 3.11.

$$h(\tau^{'}, t) = \mu(t)\delta(\tau^{'} - \tau_0^{'}). \tag{3.11}$$

Channels described by equation 3.11 are known as flat-fading or frequency-nonselective. These type of channels allow further simplification of the input-output model presented in equation 3.3, as shown in the following equation:

$$\begin{aligned} y_{BB}(t) &= \int_0^{\infty} h(\tau^{'}, t)x_{BB}(t - \tau^{'})\mathrm{d}\tau^{'} \\ &= \mu(t)\int_0^{\infty} \delta(\tau^{'} - \tau_0^{'})x_{BB}(t - \tau^{'})\mathrm{d}\tau^{'} \\ &= \mu(t) \cdot x_{BB}(t - \tau_0^{'}). \end{aligned} \tag{3.12}$$

Equation 3.12 illustrates how the channel distortion introduced can be modeled as a delayed version of the transmitted signal, multiplied by the stochastic process described in equation 3.10, $\mu(t)$. The specific distribution of $\mu(t)$ depends on the number of paths N, and the characteristics of c_n, f_n and θ_n. Assuming that the number of paths N approaches infinity, then the central limit theorem states that:

$$\mu(t) = \lim_{N\to\infty} \sum_{n=1}^{N} c_n \mathrm{e}^{j(2\pi f_n t + \theta_n)} \sim \mathcal{N}(0, 2\sigma_0^2), \tag{3.13}$$

where σ_0 satisfies the following equation:

$$2\sigma_0^2 = \mathrm{Var}\{\mu(t)\} = \lim_{N\to\infty} \sum_{n=1}^{N} E\{c_n^2\}. \tag{3.14}$$

As equation 3.13 illustrates, under the assumption of infinite paths causing multipath distortion with no LOS component present, the resulting channel process μ follows a Gaussian distribution. Extending this to the more general scenario in which a direct component is present leads to the μ_p channel process, as shown in equation 3.15:

$$\mu_p(t) = \mu(t) + m(t), \tag{3.15}$$

in which $m(t)$ corresponds to the line-of-sight component, modeled as a complex sinusoid $m(t) = \rho \mathrm{e}^{j(2\pi f_\rho t + \theta_\rho)}$. The direct component's amplitude is ρ, while its Doppler frequency and phase are represented by f_ρ and θ_ρ respectively. The superposition of both the multipath and direct components causes $\mu_p(t)$ to behave as another complex Gaussian process, with a time-variant mean equal to $m(t) = \mathrm{E}\{\mu(t)\}$.

Taking the absolute values of $\mu(t)$ and $\mu_p(t)$ respectively, generates new processes $\zeta(t)$ and $\chi(t)$, corresponding to the well-known Rayleigh and Rician stochastic processes. The former is described by the following expression:

$$\zeta(t) = |\mu(t)| = |\mu_1(t) + j\mu_2(t)|, \tag{3.16}$$

in which $\mu_1(t)$ denotes the in-phase component of $\mu(t)$, while $\mu_2(t)$ represents the quadrature component. The latter, that is, the LOS Rician process is modeled by:

$$\chi(t) = |\mu_p(t)| = |\mu(t) + m(t)|. \tag{3.17}$$

The deduction presented illustrates why Rayleigh and Rice stochastic processes can be employed to model multipath environments, under the assumptions presented previously.

3.2.2 Doppler Effect

All communication systems that involve motion experience a certain degree of Doppler effect. Caused by the relative speed between receiver and transmitter, this effect induces a frequency shift in the received signal. This shift arises due to the slight change in the total path length required for the signal to travel from transmitter to receiver.

It is possible to derive a relationship between the Doppler frequency shift f_D, carrier frequency f_c, relative speed v and angle of arrival θ. Due to the relative motion between transmitter and receiver, over a small window of time Δt the signal experiences a slight change in the distance traveled to reach the receiver Δd. These quantities are related through equation 3.18.

$$\Delta \mathrm{d} = v \cos\theta \cdot \Delta t. \tag{3.18}$$

The apparent phase shift observed in the received signal $\Delta\phi$ is determined as follows:

$$\Delta\phi = 2\pi v \cos\theta \cdot \Delta t \cdot \frac{f_c}{c}. \tag{3.19}$$

Finally, by using the well-known relationship between angular phase, time and frequency, the apparent frequency shift caused by the Doppler effect is determined as shown in equation 3.20:

$$f_D = \frac{1}{2\pi}\frac{\Delta\phi}{\Delta t} = f_c \frac{v}{c}\cos\theta. \tag{3.20}$$

The concept of Power Spectral Density (PSD) is a key concept for the statistical modeling of the Doppler effect. It is defined as the Fourier Transform of the autocorrelation function $r_{XX}(\tau)$ for any Wide-Sense Stationary (WSS) process $X(t)$, as seen in equation 3.21. As Salehi and Proakis state [59], the PSD models how power is distributed in a signal or stochastic process as a function of frequency.

$$S_X(f) = \mathcal{F}[r_{XX}(\tau)] \tag{3.21}$$

The statistical modeling of the Doppler effect follows a similar approach to the one employed previously for multipath in section 3.2.1, as outlined by Pätzold in [60]. It is assumed that propagation occurs in a two-dimensional plane, with the angles-of-arrival of the incident waves uniformly distributed in the $[0, 2\pi]$ interval. The following expression is found for the Doppler PSD of the diffuse components $\mu(t) = \mu_1(t) + j\mu_2(t)$, assuming an omnidirectional antenna is utilized:

$$S_{\mu\mu}(f) = S_{\mu_1\mu_1}(f) + S_{\mu_2\mu_2}(f), \tag{3.22}$$

with $S_{\mu_{\mathrm{i}}\mu_{\mathrm{i}}}$ described as:

$$S_{\mu_{\mathrm{i}}\mu_{\mathrm{i}}}(f) = \begin{cases} \dfrac{\sigma_0^2}{\pi f_{max}\sqrt{1-(f/f_{max})^2}}, & |f| \leq f_{max}, \\ 0, & |f| > f_{max}. \end{cases} \tag{3.23}$$

A full derivation of equation 3.23 can be found in Appendix 3.A of [60]. The PSD shown in this equation is also known as the Jakes PSD. A similar result can be found for the general scenario of propagation in 3D space, with the only difference being the lack of a singularity around $f = \pm f_{max}$.

However, it has been shown that the Jakes PSD is not always the best fit. In the context of aeornautical satellite channels, for example, it has been both theoretically [64] and empirically [65] proven that the Gaussian PSD serves as a better approximation. The definition of the Gaussian PSD can be found in equation 3.24 [60].

$$S_{\mu_{\mathrm{i}}\mu_{\mathrm{i}}}(f) = \frac{\sigma_0^2}{f_0}\sqrt{\frac{\ln 2}{\pi}}\mathrm{e}^{-\ln 2(\frac{f}{f_0})^2}. \tag{3.24}$$

In a more general sense, frequency-selective channels as a whole tend to deviate from the Jakes PSD, as found in [66]. In some scenarios, a frequency shifted Gaussian can adequately approximate the observed Doppler PSD [60]. This behavior is usually attributed to the non-uniform distribution of the incidence angles of far echoes generated by the environment.

Consequently, it is possible to statistically model the Doppler effect by producing a colored Gaussian noise with an appropriate PSD. The most immediately apparent method of accomplishing this is through filtering white Gaussian noise. However, another widely accepted, and potentially much simpler approach, is Rice's sum-of-sinusoids method [67]. Said method consists of utilizing a weighted sum-of-sinusoids, with appropriately selected coefficients, to deterministically generate a signal with the desired PSD.

3.2.3 Shadowing

While small-scale fading is attributed to multipath, large-scale fading is partly associated with Shadowing, a phenomenon caused by blockage from objects in the signal path, causing random fluctuations in the received signal power at a given distance, as defined by Goldsmith in [61]. Moreover, since the location, size, as well as the conductive and dielectric properties of the blocking objects are usually unknown, and can vary significantly over time, statistical models must be used to characterize the effect. The mathematical description presented in this section follows the deduction outlined by Goldsmith.

The most widely accepted model is lognormal shadowing [61, 68, 69], in which it is assumed that the ratio of transmit-to-receive power $\psi = \frac{P_t}{P_r}$ follows a lognormal distribution, as shown in equation 3.25. In stark contrast with the multipath modeled analyzed previously, lognormal shadowing has been validated mostly empirically rather than theoretically [70, 71]. Equation 3.25 shows the mathematical expression for lognormal shadowing.

$$P(\psi) = \frac{\xi}{\sqrt{2\pi}\sigma_{\psi_{\mathrm{dB}}}\psi}\exp\left[-\frac{(10\log_{10}\psi - \mu_{\psi_{\mathrm{dB}}})^2}{2\sigma^2_{\psi_{\mathrm{dB}}}}\right], \quad \psi > 0 \tag{3.25}$$

The key variables in equation 3.25 are the lognormal distribution's mean and variance in dB, $\mu_{\psi_{\mathrm{dB}}}$ and $\sigma_{\psi_{\mathrm{dB}}}$. They are defined as the mean and variance of the variable $\psi_{\mathrm{d}B}$, which

are naturally determined by calculating $\psi_{\text{dB}} = 10\log_{10}\psi$. Both $\mu_{\psi_{\text{dB}}}$ and $\sigma_{\psi_{\text{dB}}}$ are measured in decibels. In addition to this, an auxiliary variable ξ is defined as well for brevity, with $\xi = \frac{10}{\ln 10}$.

Using equation 3.25, the mean of the linear average path gain $\mu_\psi = \text{E}\{\psi\}$ is determined in the following manner:

$$\mu_\psi = \exp\left(\frac{\mu_{\psi_{\text{dB}}}}{\xi} + \frac{\sigma^2_{\psi_{\text{dB}}}}{2\xi^2}\right). \tag{3.26}$$

With a simple change of variables, it can be seen that the random variable resulting from converting ψ to decibels, ψ_{dB}, does indeed follow a Gaussian distribution, with $\mu_{\psi_{\text{dB}}}$ and $\sigma_{\psi_{\text{dB}}}$ as mean and standard deviation respectively:

$$P(\psi_{\text{d}B}) = \frac{1}{\sqrt{2\pi}\sigma_{\psi_{\text{d}B}}}\exp\left[-\frac{(\psi_{\text{dB}} - \mu_{\psi_{\text{dB}}})^2}{2\sigma^2_{\psi_{\text{dB}}}}\right]. \tag{3.27}$$

Given the definition of ψ, as $\psi = \frac{P_t}{P_r}$, the constraint $\mu_{\psi_{\text{dB}}} \geq 0$ must be satisfied. Additionally, it should be noted that the distribution's domain is $0 \leq \psi < \infty$, however, only scenarios with $\psi \leq 1$ are considered as feasible. The reason behind this assumption is that $\psi > 1$ implies that the received power is greater than the transmitted power, which is physically imposible. Consequently, the lognormal model better approximates the physical phenomenon of shadowing for larger values of $\mu_{\psi_{\text{dB}}}$, that is, $\mu_{\psi_{\text{dB}}} \gg 0$.

However, the lognormal model for shadowing is not without its limitations, despite how accurately it may represent real-world data. The main issue is related to the mathematical modeling employed, and can be observed primarily when attempting to combine this distribution with a Rayleigh or Nakagami Probability Density Function (PDF), to represent both shadowing and multipath simultaneously. As seen in equation 3.28, the resulting distribution is intractable, with no closed-form available to facilitate the analysis.

$$f_X(x) = \int_0^\infty \frac{x}{y}\exp\left(\frac{-x^2}{2y}\right)\frac{1}{y\sqrt{2\pi\sigma^2}}\exp\left[\frac{-\log(y-\mu)^2}{2\sigma^2}\right]\text{d}y. \tag{3.28}$$

Consequently, substantial research has been devoted to finding alternatives to the Rayleigh-Lognormal modeling for shadowing, including distributions such as the Rayleigh-Inverse Gaussian [72], Rayleigh-Birnbaum-Sanders [73], α-μ/α-μ composite [74], Generalized Rayleigh [75] and the K-distribution [76]. All these new approaches provide simpler analytical expressions to approximate fading channels affected by shadowing, while still closely approximating the empirically validated Rayleigh-lognormal approach.

3.3 LEO Geometry and Time-variance

Satellites in non-Geosynchronous orbits, as their name states, do not behave in a synchronous manner in relation to the Earth. Consequently, they are characterized by their relative motion

with respect to the Earth, leading to satellites only being visible for a limited amount of time for any given location on the planet's surface [77]. During this communication window, the relative motion causes the elevation angle to be time-varying, as described by equation 3.29 [49, 77]:

$$\cos\theta(t) = \frac{r\sin\gamma(t)}{\sqrt{r_E^2 + r^2 - 2r_E r\cos\gamma(t)}}, \tag{3.29}$$

where r_E constitutes the radius of the Earth, r corresponds to the radius of the satellite's orbit and $\gamma(t)$ is defined as the central angle between the point on the surface of the Earth and the sub-satellite point. This variable can be computed as follows:

$$\cos\gamma(t) = \cos\omega_f(t - t_0)\cos\gamma(t_0). \tag{3.30}$$

As described in [49], the Earth-Centered Fixed satellite angular velocity ω_F is defined as $\omega_F \approx \omega_s - \omega_E\cos\mathrm{i}$, with ω_s defined as the satellite's angular speed in the Earth-Centered Inertial, ω_E the Earth's angular rotation speed and i the inclination of the satellite's orbit with respect to the equatorial plane.

However, LEO geometry adds an additional layer of complexity. As stated in [77], in addition to having a variable elevation angle within a single communication window, the maximum elevation angle reached in each satellite pass varies as well.. All these effects in conjunction lead to a highly dynamic channel, in which the variable elevation angle has a significant impact in several aspects, such as the prevalence of shadowing and multipath, or the presence, or lack thereof, of a LOS component [7, 34].

Despite being a relatively well-known and studied phenomenon, the great variability of the channel in LEO satellite communication systems is definitely something that must be accounted for in channel models, with flexibility and time-variance being a very desirable aspect.

3.4 Channel Models for the scenario under study

As channel modeling has been studied extensively for many decades, several models have been proposed in literature. These proposals have been created to address different types of environments and system architectures. Evidently, not all channel models can be used to effectively model the Direct-to-Satellite IoT scenario using LEO nanosatellites.

In 1999, Karaliopoulos and Pavlidou [12] performed a very thorough review of existing channel models in literature that could be utilized to describe the Land Mobile Satellite channel (LMS), including statistical, analytical and empirical approaches. Although no single model is selected above the others, the authors state there is a clear tendency in the community to favor statistical approaches, specifically those of a state-oriented nature, over global modeling approaches. It is worth noting, that this work does not make any distinction over the type of orbit or satellite utilized, when describing the channel models.

A similar, more recent work was published by Saeed et al. [13], aiming to analyze the state of the art of the different aspects involved in CubeSat communications. These range from constellation sizing and architectures, to modulation and coding schemes. In said work, an entire section is devoted to the description of ten models that are considered as suited to represent CubeSat communication links, particularly in LEO. Multipath and shadowing as identified as the key physical phenomena in LEO CubeSats channels, with Doppler being mentioned as a very prominent effect as well.

Based on these works and other published research relevant to the task at hand, six models were initially assessed as potentially applicable to the scenario under study. The following subsections provide a detailed description and analysis of these channel models.

3.4.1 Loo's Model

Loo's model [5] is widely considered as one of the standard classical models for the LMS scenario [45, 78, 79]. It was proposed in 1985 by Chun Loo, initially conceived to model satellite links in rural environments. Consequently, Loo's model contemplates the presence of both LOS and multipath components. The channel process associated with this model is shown in equation 3.31:

$$x_{Loo} = S\mathrm{e}^{j\theta} + R\mathrm{e}^{j\phi}. \tag{3.31}$$

In equation 3.31, S follows a lognormal distribution, while R follows a Rayleigh PDF. The phases θ and ϕ are uniformly distributed over $[0, 2\pi]$. The first term represents the LOS component, affected by lognormal shadowing. The second addend, on the other hand, is used to model multipath distortion. The resulting pdf for the fading amplitude x is a rather complicated expression, as seen in the following equation [5]:

$$p(x) = \frac{x}{b_0\sqrt{2\pi \mathrm{d}_0}} \int_0^\infty \frac{1}{z} \exp\left[-\frac{(\ln(z) - \mu)^2}{2\mathrm{d}_0} - \frac{(x^2 + z^2)}{2b_0} \right] I_0\left(\frac{xz}{b_0}\right) \mathrm{d}z, \tag{3.32}$$

where μ and d_0 and correspond to the mean and variance of the log-normally shadowed LOS component S, while b_0 is defined as the power of the multipath component R. On the other hand, I_0 is the modified Bessel function of the first kind and of zeroth order.

The author evaluates the proposed model under two different practical scenarios, referred to as light and heavy shadowing. The former corresponds to measurements taken under sparse tree cover, while the latter is associated with heavy tree cover. By fitting the obtained experimental data, different sets of parameters are found for the light and heavy shadowing scenarios. Numerical evaluation of the resulting PDFs show a good degree of adjustment to both sets of experimental data. Additionally, data consisting of a combination of light and heavy shadowing is further analyzed, serving as an overall approximation of the model's performance in practice. In this final evaluation, the fit is rather poor around the median region, while remaining relatively close to the experimental values around low signal amplitudes.

The main advantage of Loo's channel model is it's relative simplicity, while still incorporating the effects of multipath and shadowing. However, it is not inherently dynamic, since the proposed model does not account for time-varying behavior in the environment. It also does not account in any way for the Doppler effect.

3.4.2 Lutz *et al.*'s Model

Similar to Loo's channel model, Lutz's proposal [6] is also considered as one of the classical LMS channel models [45,80]. Conceived in 1991, this model was designed to represent links to geostationary satellites in urban scenarios, which are characterized by short communication windows free of obstructions (i.e.: in street intersections) interspersed with intervals of heavy shadowing, mainly due to buildings and other large obstacles. The aforementioned dichotomic behavior present in urban environments is captured through a simple, two-state Markov model.

The "Good" state is used to represent windows of unshadowed communication through a Rician distribution, accounting for the presence of a direct LOS component in the received signal. The "Bad" state, on the other hand, is associated with Rayleigh-lognormal fading, to account for the lack of LOS, multipath, and heavy shadowing. The proportion of time in which heavy shadowing is present, and thus, the channel state can be considered to be in the Bad state, is captured in a Shadowing time-share variable. The distribution of the resulting signal is then expressed as a weighted sum of both Rician and Rayleigh-lognormal PDFs, in which the weighting coefficient A, denominated time-share of shadowing, is determined by best-fitting of experimental measurements. The overall PDF of the model proposed by Lutz is shown in equation 3.33 [6]:

$$p_{Lutz}(X) = (1 - A) \cdot p_{\text{Rice}}(X) + A \cdot \int_0^\infty p_{Rayl.}(X|X_0) p_{LN}(X_0) \mathrm{d}X_0, \tag{3.33}$$

where A represents the time-share of shadowing, X is the instantaneous power (random variable of the PDF) and X_0 corresponds to the mean received power. p_{Rice}, $p_{Rayl.}$ and p_{LN} correspond to Rician, Rayleigh and lognormal PDFs respectively.

The dynamic model shown in figure 3.3 captures the behavior of Lutz's proposed channel model. A spectrally-shaped complex Rayleigh process is used to generate the fading signal for both channel states. After spectrally shaping the input, the signal branches to the left and right paths, representing Good and Bad Channel States respectively, where processing is performed to obtain the desired distributions for both states.

On the Good Channel side, the Rayleigh signal is scaled by a factor of $\frac{1}{\sqrt{c}}$, after which a flat constant is added to it, representing the LOS component present in this state. Consequently, the resulting signal on the left path follows the desired Rician distribution.

To obtain the desired distribution on the Bad Channel side, a multiplication with a Lognormal-distributed variable with parameters μ and σ is performed. This operation is meant to encapsule the shadowing behavior present in the Bad state. The output of this operation follows the previously described Rayleigh-lognormal distribution.

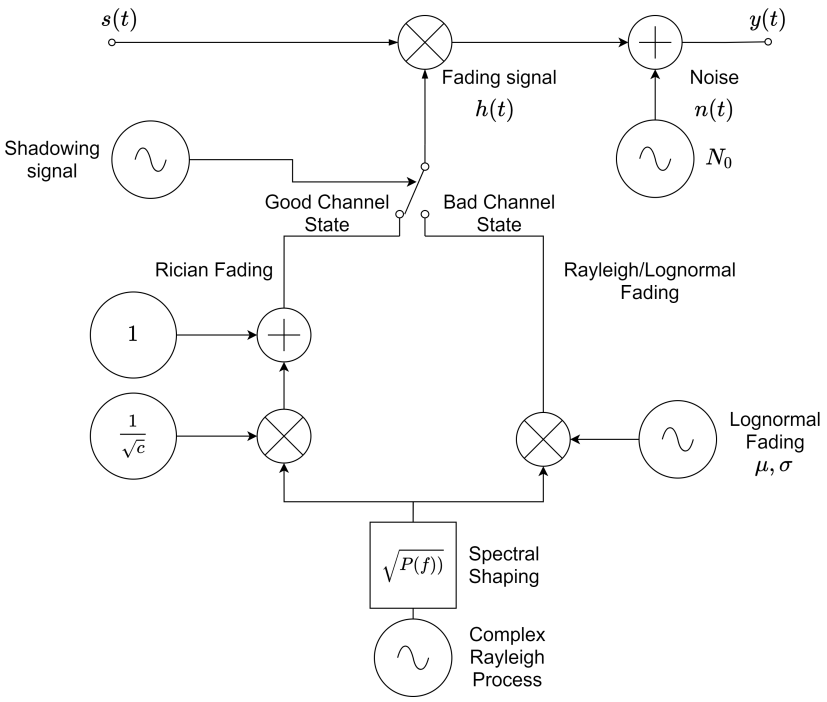

Figure 3.3: Diagram representing the two-state Markov model proposed by Lutz. The left path represents the Good state, while the right path corresponds to the bad state under heavy shadowing. Adapted from [6]

The transition between states in the model is handled by the switching process, controlled by the Shadowing Signal. This signal is generated following the Markov chain's transition probabilities p_{gg}, p_{gb}, p_{bg} and p_{bb}. Since electromagnetic fields produced by Geostationary satellites are stationary, the node's terrestrial speed and the mean "length" in meters of the bad and good states (which can be measured experimentally) can be used to deduce the mean duration of good and bad states in seconds. Consequently, the equations below can be employed to determine the aforementioned transition probabilities of the Markov chain:

$$p_{gg} = 1 - p_{gb}, \tag{3.34}$$

$$p_{gb} = \frac{v}{D_g[m] \cdot R}, \tag{3.35}$$

$$p_{bg} = \frac{v}{D_b[m] \cdot R}, \tag{3.36}$$

$$p_{bb} = 1 - p_{bg}, \tag{3.37}$$

where v is the node's speed in [m/s] and R represents the transmission rate used in [bits/s]. D_g and D_b, on the other hand, correspond to the mean duration in terms of distance of bad and good states, measured in [m].

The values of transition probabilities obtained for the Markov chain approach can be compared to the ones obtained by fitting experimental data, as described in [6]. This serves to determine how well the Markov model approximates the selected scenario.

3.4.3 Akturan *et al.*'s model

Akturan et al. presented in 1995 [7] a different approach to tackle the problem of satellite Channel modeling in urban environments, specifically devised to fit experimental L-band satellite fade measurements. Created under the assumption that distinct signal levels can be mapped to three propagation states, clear LOS (C), shadowed by trees (S) and blocked by buildings (B), the model is presented as a weighted sum of three different PDFs, each one introduced to model a different propagation state: Rice (C), Loo (S) and Rayleigh (B). The resulting PDF follows equation 3.38:

$$p_{Akturan}(X) = C \cdot p_{\text{Rice}}(X) + S \cdot p_{Loo}(X) + B \cdot p_{Rayleigh}(X). \tag{3.38}$$

Fading measurements were taken in different urban environments in Japan, with an associated elevation angle of 32°. To extend the study to a broader array of elevation angles, images taken from 236 fisheye lens placed in different cities in the country were analyzed through photogrammetry, to determine what portion of the earth-satellite link was either clear, shadowed or blocked. By recalculating these C, S and B percentages for every 5° elevation angle increment, a channel characterization of urban Japan with respect to the elevation angle was obtained, as presented in Table 2 of [7].

Despite not originally intended to model dynamic behavior in Earth-to-satellite links, the elevation angle dependency can be used to construct time-variable channels for non-Geostationary scenarios. By determining how the elevation angle varies with time in non-stationary links with satellites, a dynamic time-varying channel model can be deduced from Akturan's proposal. Such a proposal would allow all three propagation states to be present throughout the communication window, with variable weighting coefficients. This behavior is illustrated in equation 3.39, in which the time dependence is explicitly stated:

$$p_{Akturan}(X,t) = C(t) \cdot p_{\text{Rice}}(X) + S(t) \cdot p_{Loo}(X) + B(t) \cdot p_{Rayleigh}(X). \tag{3.39}$$

3.4.4 Hwang *et al.*'s model

Various models stemmed from Loo's original proposal, building upon the existing framework to enhance various aspects of it. Hwang et al.'s model in particular [8] is built as an extension of the Corazza-Vatalaro Model [79], which instead of including lognormal shadowing exclusively for the direct component, incorporates an identical shadowing component for the LOS and multipath components. Hwang et al.'s contribution in their model corresponds to the fact that the shadowing processes affecting both components are independent, and can even possess different statistical parameters.

The modifications introduced by the authors in [8], allow their model to represent a wider variety of applications, as demonstrated by the experimental validations performed in MEO and LEO-based systems. It is worth mentioning, however, that despite the fact that lognormal shadowing can be employed to model both urban and rural scenarios, the authors' focus is certainly on the latter, as all their measurements are taken in rural, tree-shadowed environments.

The modifications introduced by the authors in [8], allow their model to represent a wider variety of applications, as demonstrated by the experimental validations performed in MEO and LEO-based systems. This is in part due to the great flexibility of the lognormal shadowing approach, which can be employed to accurately represent said phenomenon in both urban and rural scenarios. However, the authors certainly focus on the latter, as all efforts to perform experimental validations are conducted in rural, tree-shadowed environments.

Equation 3.40 describes the stochastic channel process associated with Hwang's proposal:

$$r_{Hwang} = A_c S_1 \mathrm{e}^{j\theta} + R S_2 \mathrm{e}^{j(\theta+\phi)}, \tag{3.40}$$

where A_c is a constant that captures the LOS signal's power before shadowing, S_1 and S_2 are independent lognormal-distributed variables, with potentially different sets of statistical parameters, and R follows a Rayleigh distribution, representing the multipath diffuse component. Finally, θ and ϕ are uniformly distributed variables in the $[0, 2\pi]$ interval that represent the phases of the respective variables.

One noteworthy fact about Hwang at al.'s proposal is its many degrees of freedom, allowing various models based on Loo's to be considered as special cases of the former. Consequently, with appropriate parameter selection, the Hwang model can appropriately represent scenarios in which Loo's or Corazza-Vatalaro's models exhibit good results. Regarding its limitations, the model has no innate way of accounting for dynamic scenarios, due to its static nature. In addition to this, the Doppler Effect is not included in any way in Hwang's proposal.

3.4.5 Pätzold *et al.*'s model

Pätzold's model [9] is also constructed as an extension of Loo's proposal, accounting once again for the effects of multipath and shadowing. This model is set apart by two key distinctive qualities. The first one consists of allowing the in-phase and quadrature signals that comprise the diffuse multipath component to be cross-correlated, to achieve a better fit of experimental data. Said cross-correlation translates to the frequency domain as an asymmetrical Doppler Power Spectrum. The other distinctive element of the model corresponds to the explicit inclusion of the Doppler effect in the LOS component.

Both effects add additional degrees of freedom to Loo's original proposal, allowing the resulting Pätzold channel model represent more accurately real-world data. It is worth highlighting that the inclusion of the Doppler effect is particularly relevant for LEO deployments, characterized by the high relative speeds between transmitter and receiver, as outlined in section 3.2.2.

The associated random process for this model's channel fading is shown in equation 3.41:

$$r_{Patzold} = S\mathrm{e}^{j(2\pi f_p t + \theta_p)} + x_1 + j y_1, \tag{3.41}$$

where S is a lognormally distributed Shadowing variable, while the Doppler shift's corresponding frequency and phase are captured in variables f_p and θ_p respectively. On the other

hand, x_1 and y_1 correspond to the real and imaginary components of the diffuse portion, both being Gaussian-distributed, and potentially correlated. The analytical model representing Pätzold's proposal is presented in figure 3.4.

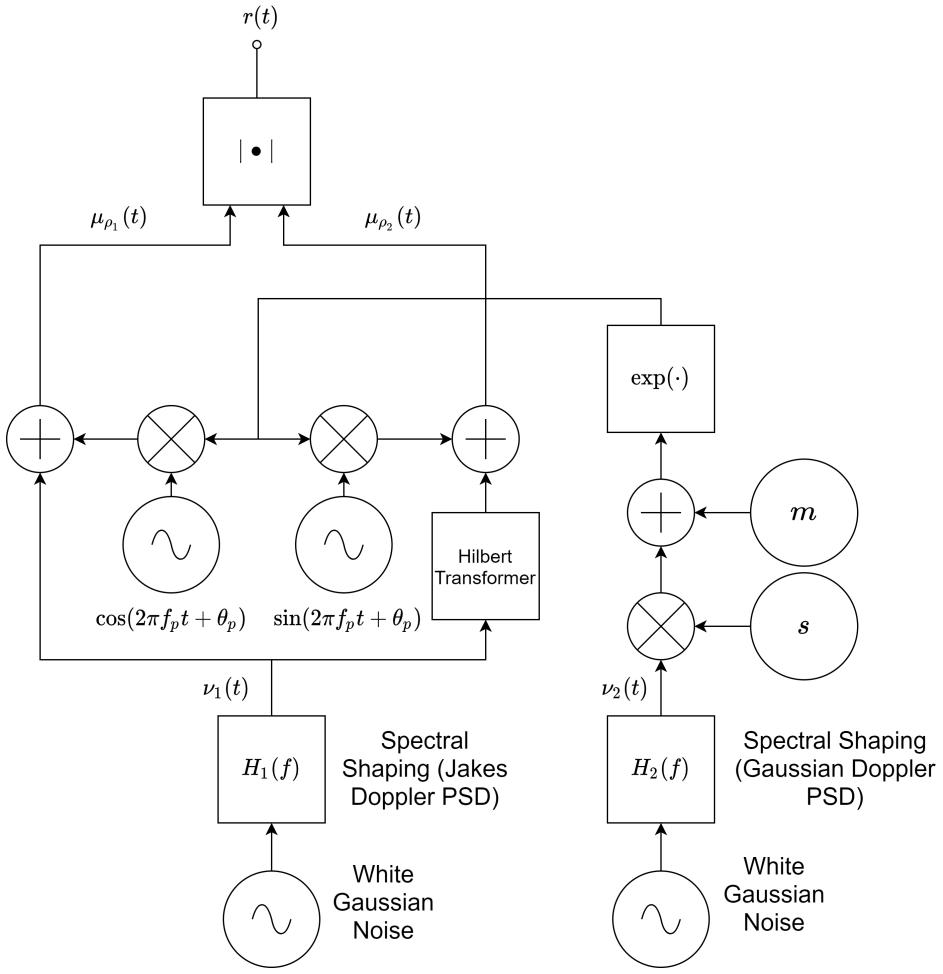

Figure 3.4: Analytical model for Pätzold's mobile channel, adapted from [9].

The Doppler PSDs associated with $\nu_1(t)$ and $\nu_2(t)$ correspond to the Jakes and Gaussian PSDs respectively. The former is employed to represent the frequency spread introduced by multipath components and the Doppler effect, while the latter serves to capture the lognormal shadowing phenomenon caused by obstructions in the environment. After adding the Doppler shift to the LOS component as well, represented in the diagram by sine waves with frequency f_p and phase θ_p, the resulting complex signal $r(t)$ is obtained, following the expression shown previously in equation 3.41.

In addition to the channel model itself, Pätzold's work introduces another noteworthy element. In the computer simulations performed to empirically validate the proposal, instead of simulating gaussian noise and filtering it to obtain the desired PSD, a sum of sinusoids approach is employed, to obtain an approximation of the target spectral characteristics. Equation 3.42 describes how $\tilde{\nu}_1(t)$ and $\tilde{\nu}_2(t)$, approximations of $\nu_1(t)$ and $\nu_2(t)$ respectively, are constructed:

$$\tilde{\nu}_{\mathrm{i}}(t) = \sum_{n=1}^{N_{\mathrm{i}}} c_{\mathrm{i},n} \cos(2\pi f_{\mathrm{i},n} t + \theta_{\mathrm{i},n}), \qquad \mathrm{i} = 1, 2 \tag{3.42}$$

where N_{i} corresponds to the number of sinusoids used for the approximation, while variables $c_{\mathrm{i},n}$, $f_{\mathrm{i},n}$ and $\theta_{\mathrm{i},n}$ represent the discrete Doppler coefficients, frequencies and phases respectively. With appropriate parameter selection, and a sufficiently high number of sinuoids, a deterministic approximation can be employed to model the stochastic process presented in equation 3.41.

While the model itself is designed to be stationary, a dynamic extension of the approach proposed by Pätzold is briefly mentioned in his work as well. The time-varying approach consists of a two-state Markov chain of two Pätzold models with different sets of parameters. While relatively simple in nature, such an approach could in fact be employed to account for time-variance in dynamic scenarios.

3.4.6 Lopez-Salamanca *et al.*'s model

Proposed in 2020, Lopez-Salamanca et al.'s Finite State Markov Chain - Two-Sectors (FSMC-TS) model [11] introduces a novel approach to channel representation in LEO scenarios. Designed from the ground up to represent LEO satellite systems, this model incorporates physical phenomena such as multipath and the Doppler effect, as well as geometrical elements of these types of orbits.

At its core, the FSMC-TS model is built around the idea of dividing the communication window between satellite and terrestrial nodes in two sectors, based on the elevation angle observed at each point in time. The assumption behind this concept is that at lower elevation angles, the effects of the physical channel are more pronounced and cause further degradation in the system.

Each sector is characterized by a K-state Finite-State Markov Chain (FSMC) constructed through PDF partitioning, based on the methodology described in [81]. This method provides a simple representation of each sector using a series of Binary Symmetric Channels (BSC). The transitions between the two sectors are deterministic, and are triggered whenever the observed elevation angle between satellite and terrestrial node crosses a given threshold. Figure 3.5 illustrates how the FSMC-TS model is constructed.

The B-sector is characterized by low elevation angles, that is, angles below the aforementioned elevation angle threshold. Consequently, this sector is intended to capture the high degree of shadowing and multipath, as well as the lack of a direct LOS component that characterize the observed channel at low elevation angles. The effects of multipath and the Doppler shift are represented through a Rayleigh PDF for the channel fading process, as described previously in section 3.2.1. Shadowing, however, does not seem to be included in the mathematical model proposed by the authors.

The Good (G) sector, on the other hand, ias associated with elevation angles above the previously mentioned threshold. In the G sector, the channel conditions are assumed to be

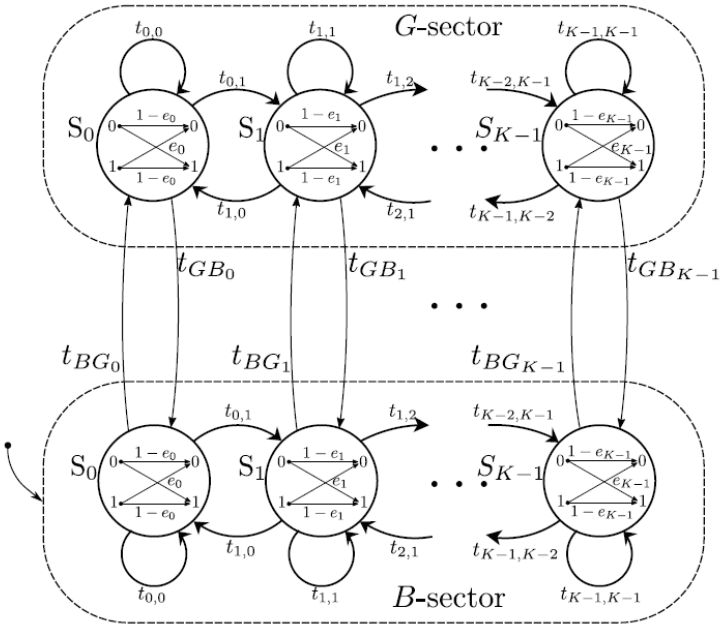

Figure 3.5: Diagram of Salamanca at el.'s FSMC-TS model. Taken with permission from [11].

significantly more favorable than in its B sector counterpart. One of the notable differences is the presence of a LOS component in the received signal, while still being affected to a certain degree of multipath distortion. The Nakagami-m distribution is proposed to represent the corresponding channel fading, in which the m parameter, referred to as the fading figure, determines the degree of prevalence of the LOS component in the received signal. It is worth mentioning that the Nakagami-m distribution is built in such a way that for values of m in the range of $\frac{1}{2} \leq m \leq \infty$, different fading scenarios can be represented. For example, for $m = \frac{1}{2}$ and $m = 1$, Gaussian and Rayleigh fading can be obtained respectively, while for larger values, fading becomes less and less severe. As $m \longrightarrow \infty$, the Nakagami-m channel converges to a non-fading one [11].

Each sector's FSMC is constructed through PDF partitioning, and requires calculating a series of parameters that determine the chain's behavior. The first step in the process is threshold calculation. A set of $K + 1$ threshold values are calculated to define K nonoverlapping intervals. These intervals are then mapped to define the K states of the respective sector's FSMC. By forcing all steady-state probabilities π_{n_k} to be equal, the threshold values can be determined by solving equation 3.43;

$$\pi_{n_k} = \int_{\Gamma_{n_k}}^{\Gamma_{n_{k+1}}} p_{\Gamma_n}(\gamma) \mathrm{d}\gamma = \frac{1}{K}, \tag{3.43}$$

where $n = B, G$ corresponds to the Bad and Good sector respectively, p_{Γ_n} represents the Rayleigh and Nakagami-m PDF respectively, $k = 0, 1, 2, ..., K - 1$ is the index variable for a total of K states, and π_{n_k} corresponds to the k-th threshold value of the Bad and Good Sector, depending on the value of n. The threshold values to be determined are mapped to variables Γ_{n_k}. After the thresholds are calculated, the associated level crossing rate N_{n_k} and

transition probabilities between states $t_{n_{\mathrm{i},j}}$, with $\mathrm{i}, j = 0, 1, 2, ..., K-1$, are determined, in equations 3.44 through 3.47.

$$N_{n_k} = \frac{\sqrt{2\pi}}{\Gamma(m)} f_{n_{D,\max}} \left(\frac{m}{\bar{\gamma}}\Gamma_{n_k}\right)^{m-\frac{1}{2}} \exp\left(\frac{m}{\bar{\gamma}}\Gamma_{n_k}\right) \tag{3.44}$$

$$t_{n_{k,k+1}} \approx \frac{N_{n_{k+1}}}{\pi_{n_k} R_s}, \qquad k = 0, 1, ..., K-2 \tag{3.45}$$

$$t_{n_{k,k-1}} \approx \frac{N_{n_k}}{\pi_{n_k} R_s}, \qquad k = 1, 2, ..., K-1 \tag{3.46}$$

$$t_{n_{k,k}} = 1 - t_{n_{k,k-1}} - t_{n_{k,k+1}}. \qquad k = 1, 2, ..., K-1 \tag{3.47}$$

In equation 3.44, N_{n_k} corresponds to the level crossing rate associated with threshold Γ_{n_k} of sector $n = B, G$, $\Gamma(m)$ is the complete gamma function evaluated in the Nakagami-m distribution fading figure m, $\bar{\gamma}$ is the average SNR value and $f_{n_{D,\max}}$ is the maximum Doppler frequency for each respective sector. In equations 3.45, 3.46 and 3.47, N_{n_k} is the level crossing rate calculated with the previous equation, π_{n_k} represents the steady-state probability of the k-th state of the Bad or Good sector, and R_s corresponds to the system's bit transmission rate.

The last set of parameters required are the bit error probability of each state's BSC. Equations 3.48 illustrate how these parameters are calculated for the two sectors:

$$\mathrm{e}_{n_k} = \frac{1}{\pi_{n_k}} \left(\beta_{n_k} - \beta_{n_{k+1}}\right), \tag{3.48}$$

where the expression for the bit error probability is described in terms of β_{n_k}, with varying expresions for the Bad and Good sector, as seen in equations 3.49 and 3.50.

$$\beta_{B_k} = \exp\left(\frac{-\Gamma_{B_k}}{\bar{\gamma}}\right)\left[1 - \Phi\left(a\sqrt{\Gamma_{B_k}}\right)\right] + \sqrt{\frac{a^2\bar{\gamma}}{a^2\bar{\gamma}+2}}\Phi\left(\sqrt{\Gamma_{B_k}\left(\frac{a^2\bar{\gamma}+2}{\bar{\gamma}}\right)}\right), \tag{3.49}$$

$$\beta_{G_k} = F_{\Gamma_G}(\Gamma_{G_k})\left[1 - \Phi\left(a\sqrt{\Gamma_{G_k}}\right)\right] + I_k. \tag{3.50}$$

I_k is defined in equation 3.51. Γ_{B_k} and Γ_{G_k} correspond to the k-th threshold value for the Bad and Good sectors respectively, Φ represents the CDF of the Gaussian distribution, F_{Γ_G} corresponds to the CDF of Γ_G (Nakagami-m distribution), a is a parameter specific to the modulation scheme employed and γ_k is the incomplete gamma function.

$$I_k = \frac{1}{2\sqrt{\pi}\cdot\Gamma(m)} \sum_{\mathrm{i}=0}^{\infty} \left[(-1)^{\mathrm{i}} \frac{\left(\frac{m}{\bar{\gamma}}\cdot\frac{2}{a^2}\right)^{m+\mathrm{i}}}{\mathrm{i}!(m+\mathrm{i})} \cdot \gamma_k\left(m+\mathrm{i}-\frac{1}{2}, \frac{a^2}{2}\Gamma_{G_k}\right)\right]. \tag{3.51}$$

The FSMC-TS model implicitly assumes that transitions are only possible between adjacent states, that is, $t_{n_{\mathrm{i},j}} = 0, \quad \forall j \notin \{\mathrm{i}-1, \mathrm{i}, \mathrm{i}+1\}$, as seen in equations 3.45, 3.46 and 3.47. Additionally. since $t_{n_{k,k+1}}$ and $t_{n_{k,k-1}}$ are estimated as a quotient of the Level Crossing Rates (LCR) N_{n_k} and bit transmission rate R_s, the approximations presented are only valid for high enough values of bit transmission rates. For low bit rates, the channel fading presents a substantial degree of variability over the transmission of a single bit. To fit these types of scenarios, the model would need to be extended to allow transitions between states other than just adjacent ones.

3.5 Evaluating and selecting a channel model

The analysis performed so far has been almost exclusively descriptive. All models have been described in detail from a theoretical and analytical standpoint, but no attempt has been made to evaluate and/or compare them. To properly assess which channel models are best suited to represent the scenario at hand, a methodology that captures the requirements of an adequate channel model must be defined. Chapter 4 introduces a methodical framework created to evaluate and rank the six models described in this chapter.

Chapter 4

Framework for Channel Model Comparison and Analysis

4.1 Framework overview

The six models previously described in section 3.4 serve as prime candidates for the Direct-to-Satellite IoT deployment scenario, supported by LEO nanosatellites. To continue the analysis of these models and allow a fair evaluation and comparison of each approach, a proper framework needs to be defined. Said framework should be a replicable, methodical approach to model analysis, incorporating the inherent limitations and challenges of the scenario under study, in addition to including experimental validation of each evaluated model's performance. The rest of this chapter builds upon the work published previously in [82].

The proposed framework is comprised of the following steps: 1) define a set of evaluation criteria that are in line with the requirements identified in section IV, which are then utilized to construct a weighted score metric that allows the shortlisting of a subset of models; 2) perform a comparative analysis via simulations with model parameters selected to be representative of the DtS-IoT scenario using LEO nanosatellites; and 3) test the selected models in a Hardware-in-the-Loop (HITL) setting that allows validaton of the shortlisted models in a more realistic context. Figure 4.1 visually represents the methodology defined for the proposed framework.

Figure 4.1: Diagram illustrating the three-step methodology defined to analyze channel models for the DtS-IoT supported by LEO nanosatellites scenario. *Step 3 is left for future work, and is outside of the scope of this thesis.*

The first step of the process, 'Weighted Score Assessment', consists of a qualitative evaluation of each model utilizing a set of criteria to calculate a weighted score metric. These criteria are defined to capture the requirements that need to be satisfied by an appropriate channel model in three areas: (1) the accuracy to which physical phenomena are being modeled mathematically, (2) the degree to which the model captures dynamic behavior (i.e.: time-variant) and finally, (3) the computational complexity associated with the model. The resulting weighted score is utilized to once again pre-select a subset of models as potential candidates, which are considered to be suitable for further analysis. Section 4.2.1 describes the methodology of this step in greater detail.

Following that, the pre-selected models from the initial step are comparatively analyzed using computer simulations. Through the Monte Carlo method, samples are generated from each model's associated distribution. These samples are then utilized to compare the channel models at a basic statistical level. These direct comparisons shed some light as to how each model would perform in the DtS-IoT scenario utilizing LEO nanosatellites. Section 4.3.1 provides a in-depth explanation of the methodology of step 2.

Finally, models are put to the test in an empirical manner through HITL simulations. This step of the process allows evaluation each model's performance, using Bit Error Rate (BER) as a metric, for example, in a more realistic environment. The methodology proposed consists of utilizing Software Defined Radios (SDR) as transmitters and receivers, simulating the effect of the channel using MATLAB or Simulink. Additionally, other mechanisms employed in a satellite communications can be added to the simulation loop, such as channel coding or retransmission schemes, to further improve the accuracy of the communication system simulated, as shown in [11]. The third and final step of the process is not performed as part of the work described in this thesis, and is considered to be future work, as stated later in section 6.2.

4.2 Weighted Score Assessment

4.2.1 Methodology

The methodology employed as part of the weighted score assessment is covered in this section. As stated previously, the main objective of this step is to utilize a qualitative analysis in conjunction with a weighted score metric to narrow down the list of candidate models. To this effect, criteria $C1$, $C2$ and $C3$ are defined, each aiming to cover a different element of the scenario under study.

The incorporation of the three key physical phenomena outlined in section 3.2, multipath, the Doppler effect and shadowing, is essential. As seen in the channel model descriptions in section 3.4, there are significant differences in the way each channel handles the modeling of physical phenomena, with some approaches foregoing certain phenomena altogether. Consequently, the first criterion attempts to measure to which degree the key physical effect of LEO satellite channels are captured by the mathematical representation of each channel model, aptly named $C1$: Inclusion of key physical phenomena.

Another very important aspect of LEO satellite channels corresponds to the highly dy-

namic nature of the environment, as highlighted in section 3.3. Due to the time-varying nature of the LEO satellite link, the degree to which the channel causes signal degradation varies greatly throughout the communication window. These changes range from a shift from NLOS to LOS conditions, to variations in the multipath, Doppler and shadowing magnitude present in the channel. Therefore, approaches that prove to be time-varying in nature are preferred over static ones. Generally, this leads to multi-state modeling channels having an inherent edge over global modeling channels. Criterion $C2$: Degree of dynamism, aims to capture this aspect of the task at hand.

Finally, one of the biggest limitations stemming directly from the usage of nanosatellites/CubeSats, corresponds to the scarcity of on board processing power available. Despite the fact that more sophisticated models may prove to more accurately represent the scenario under study, the constraint on available processing power implies that arbitrarily complex approaches are not feasible to implement in a real-world scenario. This is a limitation to consider not only for simulation purposes, but also due to the fact that if any channel information is intended for use at the upper layers, the complexity of calculations for channel measurement and parameter estimation must be kept with bounded complexity. Criterion $C3$: Computational Complexity, aims to measure this element of the channel models.

$C1$, $C2$ and $C3$ are assigned an integer value from 1 to 3, with a higher score being associated with a better model evaluation. The three criteria just described are summarized below:

C1 Inclusion of key physical phenomena: multipath, doppler effect, and shadowing. A high score means the phenomena are modeled in a more complete manner.

C2 Degree of dynamism: A higher score means the model captures the time-variant nature of the problem in a more complete or effective manner.

C3 Computational complexity: A higher score means the model is less reliant on available processing power.

With the criteria defined, a weighted score value is calculated for each model, as shown in equation 4.1:

$$WS = w_1 \cdot C1 + w_2 \cdot C2 + w_3 \cdot C3. \tag{4.1}$$

This approach provides a simple yet flexible mechanism to aggregate the values of all three scores, allowing direct ranking and comparison between models. Depending on how the coefficients are selected, the three dimensions of the problem can be prioritized differently. As an initial approach to model evaluation, the selected values for the coefficients in this work are: $w_1 = w_2 = 2$ and $w_3 = 1$. The reasoning behind this decision is that the model's ability to represent the relevant physical phenomena and incorporate time-variance are considered to be much more relevant than its computational complexity. As mentioned previously, the impact of a higher computational complexity affects mainly simulations, especially HITL scenarios, and potential applications in upper layer protocols utilizing channel information to make decisions. Since none of these issues correspond to the focus of this thesis, criterion

$C3$ is given a comparatively smaller weight in the calculation of WS.

After having calculated the resulting WS for all channel models, the three highest scores out of the six total are pre-selected for further analysis, proceeding to step 2 of the Channel Model Comparison and Analysis Framework. The methodology employed for the comparative simulations is described in section 4.3.1.

4.2.2 Results and analysis

The values assigned for $C1$, $C2$ and $C3$, along with the final scores are provided for each model in table 4.1. A breakdown for each criterion is provided below.

Table 4.1: Weighted Score of selected channel models for DtS-IoT scenarios. An additional row is added to include a theoretical Enhanced FSMC-TS model, incorporating the effects of Shadowing.

Model	**C1**	**C2**	**C3**	**WS**
Loo [5]	1	1	3	7
Lutz [6]	1	2	2	8
Akturan [7]	2	3	2	12
Hwang [8]	2	1	2	8
Patzold [9]	3	2	2	12
FSMC-TS [11]	2	3	1	11
Enhanced FSMC-TS*	3	3	1	13

All models include some form of multipath, with different levels of flexibility provided with each approach. In this regard, the Loo and Lutz models definitely are most lacking, with little flexibility provided in this regard when compared to the Akturan, Hwang, Patzold and FSMC-TS channels. With respect, to shadowing, all channel models with the exception of the FSMC-TS model incorporate some form of shadowing, usually through a Rayleigh-lognormal distribution. This imposes a clear disadvantage to the FSMC-TS approach, when compared to the rest. Finally, regarding the Doppler effect, only the Patzold and FSMC-TS channels explicitly account for it as part of their mathematical models, providing a clear edge over the rest of the models. The analysis just presented leads to the values of $C1$ assigned in table 4.1. An additional row is added to the table, including a potential Enhanced FSMC-TS channel that addresses the only shortcoming of the model associated with this criterion, the lack of shadowing. This topic is covered in extensive detail in Chapter 5.

Given that the Direct-to-LEO-satellite IoT scenario is characterized by its highly dynamic nature, it is important for the selected channels to be able to introduce a certain degree of time-variance in the respective models. The Lutz, Akturan and FSMC-TS channels are the only ones to intrinsically introduce time-variance: The Lutz model through its two states (good and bad), the Akturan model through the variation of statistics every five-degree increment of the elevation angle, and the FSMC-TS model through the transition between the Bad and Good sectors based on the elevation angle observed. Despite being stationary by nature, the authors in [9] propose that the Patzold model can be extended, in a manner similar to the Lutz model, to account for time-variance by using two Patzold channels with different statistics. This analysis leads to the values of $C2$ presented in table 4.1.

The third criterion aims to impose limits on the computational complexity of each of the evaluated models, given the limitations in power and onboard processing capacity in both the nanosatellite and in the terrestrial IoT devices. This constraint is applied to reduce the impact in the implementation of physical and MAC level protocols of the system. In this regard, the clear advantage goes to the Loo, Lutz and Hwang channels, as they require the least amount of parameters and computational processing to be implemented. The FSMC-TS model in particular is quite complex, requiring substantial processing for the Markov Chain simulations and parameter estimation. Nevertheless, the hardware-in-the-loop simulations presented by Salamanca *et al.*. indicate that a practical application of the model with constrained processing power is achievable. The values assigned to this criterion $C3$ are summarized in table 4.1, based on the analysis presented.

Based on the weighted scores of all models, the three channels shortlisted as potential candidates for the scenario are the Akturan [7], Patzold [9] and FSMC-TS [11] models, with scores of 12, 12 and 11 respectively. However, it is worth noting that the theoretical Enhanced FSMC-TS channel, addressing the lack of shadowing in the FSMC-TS model, is positioned as potentially the best overall channel, with a score of 13. This serves as the main motivation for Chapter 5, in which the task of implementing shadowing in the FSMC-TS channel is tackled.

The results presented in this section illustrate the fact that each model presents a set of distinct advantages and disadvantages. Consequently, further analysis and testing is still required before being able to select a definitive model. Section 4.3 presents a first approach, using simulations, to continue the analysis.

4.3 Comparative Simulations

4.3.1 Methodology

The main objective of the experiments described in this section consists of utilizing the probabilistic representations of the pre-selected channel models to perform direct comparisons in a simulated setting. Additionally, due to it being widely considered as a baseline approach, Loo's model is included in the simulations for reference. The variables studied in these set of experiments are the mean fading amplitude α, as well as the fading amplitude's CDF, but the framework is flexible enough for other metrics to be employed as well, such as the BER to compare the models' performance.

Simulations are performed utilizing the Monte Carlo method to draw samples for each channel model utilizing two satellite elevation angles, $\theta = 0°$ and $\theta = 20°$, corresponding to the B and G sectors respectively in the FSMC-TS model. Since the Loo, Patzold and Akturan models need to be simulated as well, special care needs to be placed in parameter selection. To make sure direct comparisons are performed in a fair manner, a separate set of parameters must be calculated for the two selected elevation angles.

The parameters for the Akturan model are selected utilizing adjusting the parameters to the ones presented by the author in tables 1 and 2 of [7]. Consequently, the Akturan model's PDF is expressed through the following equation, where the dependency of the coefficients

on the elevation angle is made explicit:

$$p_x(x,\theta) = C(\theta)p_{\text{Rice}}(x) + S(\theta)p_{\text{Loo}}(x) + B(\theta)p_{\text{Rayleigh}}(x). \tag{4.2}$$

Having this set of parameters defined for the Akturan model, the other model's parameters are determined through exploration and testing of different values.

4.3.2 Results and analysis

Simulation results following the methodology described previously are presented in this section. Due to time constraints, the results presented correspond to the Loo, Akturan and FSMC-TS models only, with results for Patzold's channels being considered for future work, as described in section 6.2.

The parameters employed for the simulations are summarized in table 4.2. For the sake of simplicity, the auxiliary variables $S = 10\log_{10}(\sqrt{\mathrm{d}_0})$, $M = 10\log_{10}(\mu)$ and $MP = 10\log_{10}(b_0)$ have been defined for Loo's model, maintaining the same nomenclature as utilized previously in section 3.4.1.

Table 4.2: Simulation Parameters

	Akturan [7]			**FSMC-TS [11]**		**Loo [5]**		
θ	**C (%)**	**S (%)**	**B (%)**	**m**	$\bar{\gamma}$ **(dB)**	**S (dB)**	**M (dB)**	**MP (dB)**
0°	2	3	95	2	-18	3E-4	-20	-24
20°	36	8	56	5	-6.2	1.7	-7	-20

For the first experiment, a Monte Carlo simulation with 200 iterations is performed to calculate the mean value of the fading amplitude variation for each channel, throughout a time interval of 16×10^4 samples. Figure 4.2 shows the results obtained for the two elevation angles 0° and 20°.

Initially, it is immediately apparent that the simulations produce two groups of results, with one set of curves centered around -7 [dB], and the other around -19 [dB], for $\theta = 0°$ and $\theta = 20°$ respectively. Furthermore, across all three channels, the former group shows signicantly less variance than the latter. This result is consistent with the assumption that the effect of the channel is less detrimental at higher elevation angles.

When comparing the different channel models, the Akturan and Loo models tend to show similar degrees of variance in the Montecarlo simulations for both elevation angles, in stark contrast to the FSMC-TS model. The latter tends to exhibit much less variability with respect to time, across iterations of the Monte Carlo experiment.

Following that, a similar procedure is employed to obtain simulated fading amplitude CDFs for the Loo, Akturan, Patzold and FSMC-TS channel models. Monte Carlo simulations with 200 iterations are done, drawing a total of 16×10^4 samples each time from each model's fading amplitude distribution. Based on said samples, an empirical estimation of the CDF is obtained. The results are shown in figure 4.3, where the following curves are included:

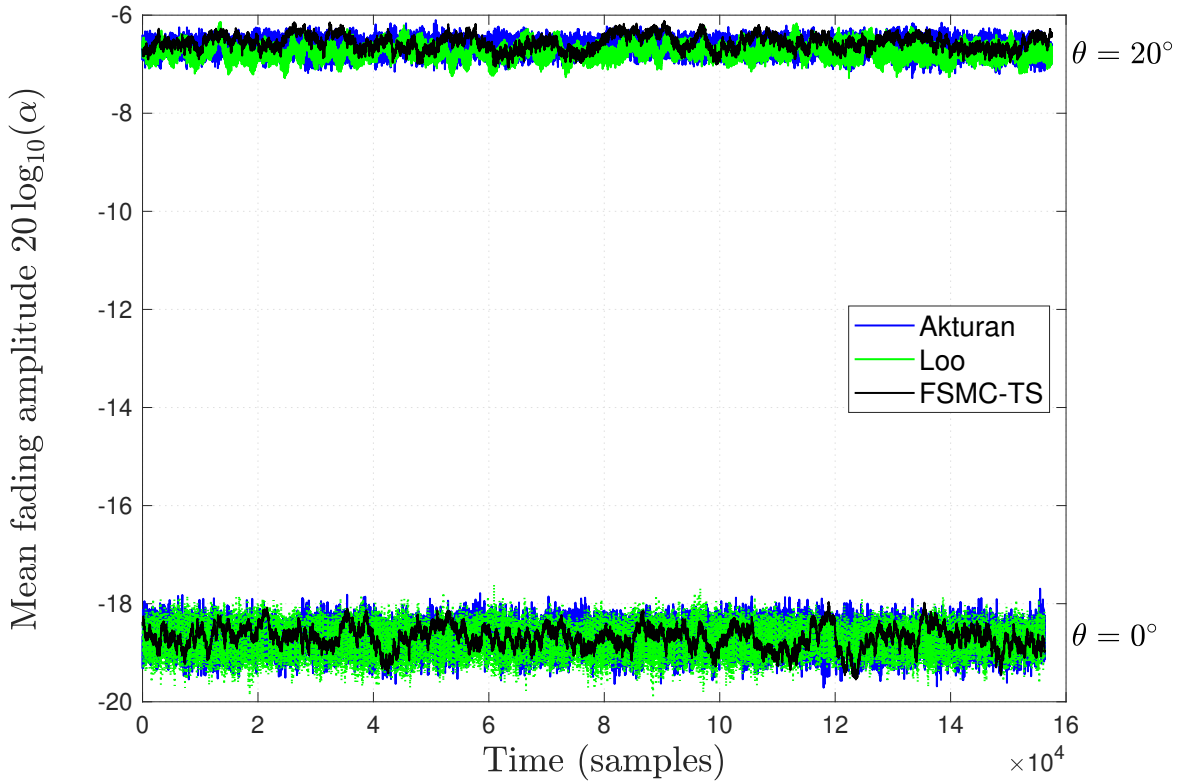

Figure 4.2: Fading amplitude variation for the Akturan's and FSMC-TS models. Loo's model included as a reference.

(*i*) the CDF for the probability distributions of the theoretical (calculated) and simulated components of the Akturan model: $p_{\text{Rayleigh}}(\alpha)$, $p_{\text{Loo}}(\alpha)$, and $p_{\text{Rice}}(\alpha)$; (*ii*) CDF of the simulated Akturan model; (*iii*) CDF of the simulated Loo model (included as reference); and (*iV*) CDF of the theoretical (calculated) and simulated FSMC-TS model. Results (*ii-iii*) are shown for the elevation angles 0° and 20°.

The results demonstrate that the Akturan model can be used to approximate variety of models by adjusting the weighting coefficients appropriately. This can be seen by observing how the different variants of the simulated Akturan model can approach the Rayleigh, Loo, and Rice components of the model, to account for a wide spectrum of channel scenarios.

Similarly, the CDF curves obtained from simulating the Loo, FSMC-TS and Akturan channels for both elevation angles studied ($\theta = 0°$ and $\theta = 20°$) show a great degree of similarity across the three models, using the parameters specified in table 4.2. Additionally, both sets of curves capture the effect that increasing the elevation angle has on channel quality, given that higher envelope magnitude signal levels become more prevalent for higher elevation angles, as discussed in [11].

Unfortunately, the simulation results presented in this section on their own are not sufficient to determine which model is more suited to fulfill the task at hand. Nevertheless, the work presented in this section serves as a first approach to evaluating the pre-selected models

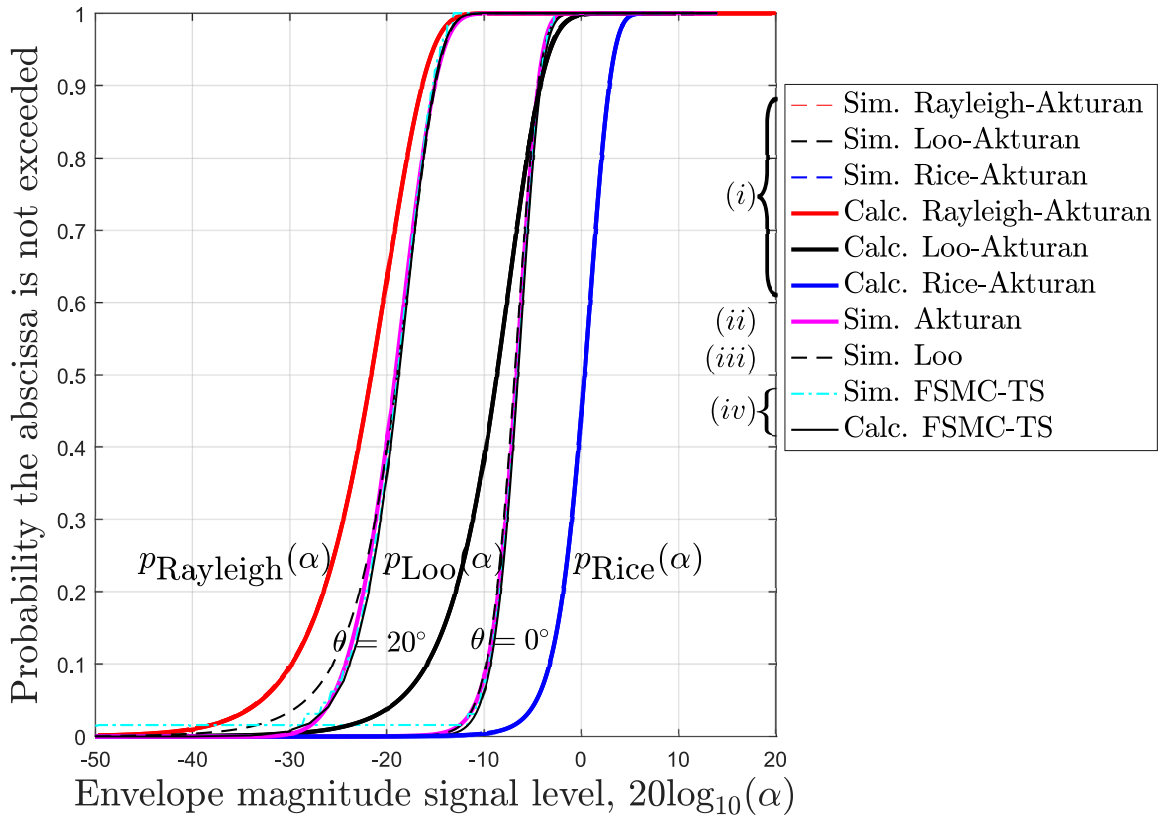

Figure 4.3: CDF of the fading amplitude for the Akturan's and FSMC-TS models. Loo's model included as a reference.

through simulations. Several avenues are available for improvement and further research, as is presented in detail in section 6.2.

Chapter 5

Enhanced FSMC-TS Channel Model

Three channel models were identified as potentially suited to represent the Direct-to-LEO satellite IoT scenario: Akturan's [7], Pätzold's [9] and Salamanca et al.'s [11] proposals. Despite possessing a clear set of strengths that set them apart, there is substantial room for improvement to make them an even better fit for the scenario under study. In this chapter, a potential enhancement to Salamanca et al.'s FSMC-TS channel is explored, looking to address its most immediately apparent limitation: the lack of shadowing in the mathematical representation employed, as highlighted previously in section 4.2.2 .

5.1 Lack of Shadowing in the B-sector

In the original FSMC-TS manuscript, shadowing is mentioned as one of the key phenomena present in LEO satellite communication systems, especially at lower elevation angles, as seen in figure 5.1. However, there is no incorporation of this effect in the mathematical modeling of the system, as outlined in section 3.4.6. This disconnect between the characteristics of the scenario under study and the mathematical modeling of the environment leads to a significant underestimation of the negative effects of the channel in the communication system. This gap presents a clear opportunity to improve to the original FSMC-TS model, potentially achieving a better representation of the desired channel conditions.

The B-sector models harsher channel conditions, where shadowing is most likely to affect the communication system. Consequently, it makes the most sense to direct any attempts to include this phenomenon toward the B-sector. Initially, the easiest and most direct approach

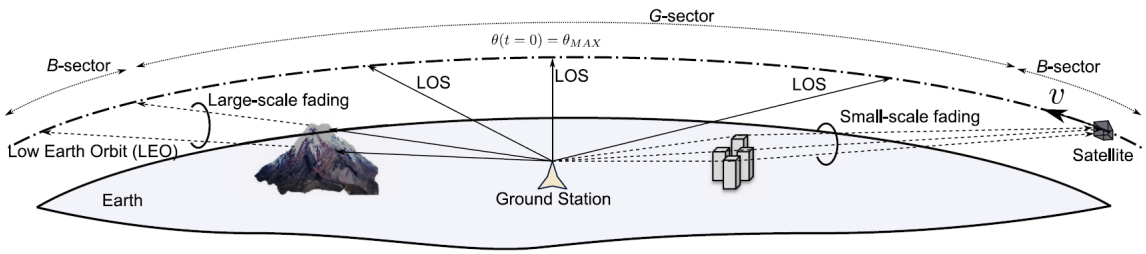

Figure 5.1: Illustration of the shadowing and multipath effects present in direct-to-LEO satellite communication systems. Extracted with permission from [11].

to accomplish this would be to add an independent Lognormal component to the Rayleigh PDF employed in this sector's Markov Chain, since it is considered to be one of the most empirically accurate methods of modeling shadowing in a probabilistic manner.

However, the mathematical intractability and high overall complexity of the resulting Rayleigh-Lognormal PDF, proves to be an important obstacle, making it very difficult to calculate this new model's FSMC parameters. Consequently, the alternative distributions mentioned at the end of section 3.2.3 prove to be very attractive alternatives. These models serve as estimates of the Rayleigh-Lognormal PDF with varying degrees of accuracy, while possessing much simpler and easier to handle mathematical representations.

The K-distribution [76] seems to be particularly promising, serving as an accurate approximation of the Rayleigh-Lognormal model. Additionally, analytical expressions can be found with relative ease for its key parameters and performance metrics, such as BER under common modulation schemes [76,83]. Moreover, an FSMC implementation of a K-fading channel is already described in [84], illustrating how some of the key parameters of the Markov Chain can be computed, such as LCR and transmission probabilities.

5.2 The K-distribution

The K-distribution can be characterized as a composition of the Rayleigh and Gamma distributions, as shown in the probability density function of the fading amplitude x, described by equation 5.1 [76]:

$$p_K(x) = \frac{2}{\alpha\Gamma(\beta+1)}\left(\frac{x}{2\alpha}\right)^{\beta+1} K_\beta\left(\frac{x}{\alpha}\right), \tag{5.1}$$

in which α and β are the distribution's parameters, and K_β corresponds to the modified Bessel function of the second kind and order β.

It is worth noting though, that the aforementioned PDF does not describe the signal's instantaneous SNR γ due to the fading channel and noise, but rather the channel's fading amplitude x. Both variables are related through the following equation, as stated in the original FSMC-TS manuscript [11]:

$$\gamma(x) = x^2\frac{E_s}{N_0} \tag{5.2}$$

Theorem 4.1 in [85] provides an expression to calculate the PDF of a function of a random variable. Equation 5.3 describes said theorem:

$$f_Y(y) = \begin{cases} \frac{f_X(x_1)}{\|g'(x_1)\|} & \text{where } g(x_1) = y \\ 0 & \text{if } \nexists x \in \mathbb{R} \mid g(x) = y, \end{cases} \tag{5.3}$$

where the function $g : \mathbb{R} \to \mathbb{R}$ defines the relationship $y = g(x)$ and is strictly increasing and differentiable.

Utilizing this theorem along with the relationship between γ and α, the following result is obtained, describing the signal SNR's PDF, $p_K(\gamma)$, as shown in equation 5.4:

$$p_K(\gamma) = \frac{2}{\Gamma(\beta+1)} \cdot \gamma^{\frac{\beta}{2}} \left(\frac{1}{4\alpha^2 \frac{Es}{N_0}} \right)^{\frac{\beta+2}{2}} \cdot K_\beta \left[2 \left(\frac{1}{4\alpha^2 \frac{Es}{N_0}} \right)^{\frac{1}{2}} \gamma^{\frac{1}{2}} \right]. \tag{5.4}$$

The complete derivation of $p_K(\gamma)$ can be found in Appendix A.

A similar analysis can be performed to obtain the instantaneous SNR's CDF $F_\gamma(\gamma)$, by utilizing the much simpler relationship between $F_x(x)$ and $F_\gamma(\gamma)$ deduced in the following equation:

$$\begin{aligned} F_\gamma(\bar{\gamma}) &= \mathbb{P}(\gamma \leq \bar{\gamma}) && (5.5)\\ &= \mathbb{P}\left(\sqrt{\frac{\gamma}{\frac{E_s}{N_0}}} \leq \sqrt{\frac{\bar{\gamma}}{\frac{E_s}{N_0}}} \right) && (5.6)\\ &= \mathbb{P}\left(x \leq \sqrt{\frac{\bar{\gamma}}{\frac{E_s}{N_0}}} \right) && (5.7)\\ &= F_x\left(\sqrt{\frac{\bar{\gamma}}{\frac{E_s}{N_0}}} \right). && (5.8) \end{aligned}$$

Equation 5.6 is obtained after applying the monotonically increasing transformation consisting of dividing by a positive number and taking the square root, while equation 5.7 is reached by using the inverse of the relationship $\gamma(x)$ defined in equation 6.2.

A closed-form equation for $F_x(x)$ is provided in [84], as seen in the following equation:

$$F_x(x) = 1 - \frac{2^{-\beta}}{\Gamma(\beta+1)} \left(\frac{x}{\alpha} \right)^{\beta+1} K_{\beta+1}\left(\frac{x}{\alpha} \right) \tag{5.9}$$

Using this expression in equation 5.8, the following result is deduced for the CDF of the instantaneous SNR $F_\gamma(\gamma)$

$$F_\gamma(\gamma) = 1 - \frac{2^{-\beta}}{\Gamma(\beta+1)} \left(\sqrt{\frac{\gamma}{\alpha^2 \frac{E_s}{N_0}}} \right)^{\beta+1} \cdot K_{\beta+1}\left(\sqrt{\frac{\gamma}{\alpha^2 \frac{E_s}{N_0}}} \right) \tag{5.10}$$

These results are then compared with the work presented in [86] and [87] for the generalized K-distribution, which, as its name suggests, is an extension of the original K-distribution. The generalized PDF is presented in the following equation:

$$p_{K_g}(\gamma) = \frac{2\,\Xi^{(\hat{\beta}+1)/2}\gamma^{(\hat{\beta}-1)/2}}{\Gamma(m)\Gamma(k)} K_{\hat{\alpha}}\left[2(\Xi\gamma)^{(1/2)}\right], \tag{5.11}$$

with $\hat{\alpha} = k - m$, $\hat{\beta} = k + m - 1$, $\Xi = (km)/\bar{\gamma}$ and $\bar{\gamma} = \Omega k \frac{E_s}{N_0}$, with Ω defined as the mean signal power. Consequently, the model is completely defined by 3 fundamental parameters: k, m and $\frac{E_s}{N_0}$. The first two are directly tied to the k distribution itself, while the latter corresponds to the normalized signal-to-noise ratio.

The expressions presented in equations 5.4 and 5.11 are proven to be equivalent when considering the special case of $m = 1$ for the latter, with the following relationship between each set of parameters:

$$\Omega = 4\alpha^2, \tag{5.12}$$
$$k = \beta + 1. \tag{5.13}$$

Unless specified otherwise, it is assumed that $\Omega = 1$, leading to $\alpha = \frac{1}{2}$ in most scenarios. On the other hand, β is left as the model's free parameter, capturing the degree of shadowing present in the channel.

After validating the obtained PDF for the instantaneous SNR with the Generalized K-fading equations [86, 87], it is possible to proceed with the FSMC implementation, intended to replace the B-sector in the FSMC-TS model [11].

5.3 K-distributed FSMC implementation

By utilizing the distribution described in equation 5.4 to model the received signal's SNR, it is possible to implement an FSMC model for the B-sector that captures the effect of the K-fading channel, as seen in [84]. This novel proposal is referred to as the Enhanced FSMC-TS channel, aiming to incorporate shadowing into the original FSMC-TS model introduced in [11]. The following set of equations summarize the necessary parameters to implement the K-fading FSMC:

$$\pi_{B_k} = \int_{\Gamma_{B_k}}^{\Gamma_{B_{k+1}}} p_K(\gamma)\mathrm{d}\gamma = \frac{1}{K}, \tag{5.14}$$

$$N_{A_{B_k}} = f_m \int_0^{\infty} \dot{\gamma} \cdot p\left(A, \dot{\gamma}\right) \mathrm{d}\dot{\gamma}, \tag{5.15}$$

$$t_{B_{k,k+1}} \approx \frac{N_{B_{k+1}}}{\pi_{B_k} R_s}, \qquad k = 0, 1, ..., K-2 \tag{5.16}$$

$$t_{B_{k,k-1}} \approx \frac{N_{B_k}}{\pi_{B_k} R_s}, \qquad k = 1, 2, ..., K-1 \tag{5.17}$$

$$t_{B_{k,k}} = 1 - t_{B_{k,k-1}} - t_{B_{k,k+1}}, \qquad k = 1, 2, ..., K-1 \tag{5.18}$$

$$\mathrm{e}_{B_k} = \frac{1}{\pi_{B_k}} \int_{\Gamma_{B_k}}^{\Gamma_{B_{k+1}}} p_K(\gamma)\mathrm{e}(\gamma)\mathrm{d}\gamma. \tag{5.19}$$

Equations 5.14 and 5.19 are solved numerically, while 5.15 can be solved analytically. Equations 5.16, 5.17, 5.18, on the other hand, can be calculated after obtaining the rest of the parameters.

While [84] defines the groundwork for the derivation of the level-crossing rate N_A, certain corrections must be made to the analysis presented. The main cause behind this is the fact that it is wrongly assumed that the fading amplitude distribution can be used to represent the instantaneous SNR PDF, instead of utilizing equation 5.2 to derive the corresponding distribution. Nevertheless, many other aspects of the authors' derivation remain valid, and are utilized in the analysis presented in this work.

To start, it is assumed that $\dot{\gamma}$ follows the same distribution as γ. Similarly, as it is considered in [88], $\dot{\gamma}$ and γ are taken to be independent, that is, $p(A, \dot{\gamma}) = p(A)p(\dot{\gamma})$. Under these assumptions, the following expression for N_{B_k} is obtained, with the complete derivation presented in Appendix B:

$$N_{B_k} = 2^{\beta+1} \cdot \frac{C_{B_k}}{D^{\beta+2}} \cdot \Gamma(\beta+1) \tag{5.20}$$

$$C_{B_k} = f_m \frac{4\Gamma_{B_k}^{\frac{\beta}{2}}}{\left(\Gamma(\beta+1)\right)^2} \left(\frac{1}{4\alpha^2 \frac{Es}{N_0}}\right)^{\beta+2} \cdot K_\beta \left[2\left(\frac{1}{4\alpha^2 \frac{Es}{N_0}}\right)^{\frac{1}{2}} \cdot \Gamma_{B_k}^{\frac{1}{2}}\right]. \tag{5.21}$$

$$D = 2 \cdot \left(\frac{1}{4\alpha^2 \frac{Es}{N_0}}\right)^{\frac{1}{2}}. \tag{5.22}$$

All left-hand side variables represent the same parameters as described in section 3.4.6. Following the procedure outlined previously, it is possible to fully implement a K-distribution based FSMC to replace the FSMC-TS channel's B-sector.

5.4 Simulation Setup

With the FSMC parameters computed, it is possible to obtain BER simulation results through Monte Carlo experiments. These consist of simulating a transmitter sending a sequence of size N of randomly generated bits through the FSMC-TS channel at different levels of SNR per symbol. Each time a bit is transmitted, uniformly generated numbers in the $[0, 1]$ interval are generated and compared to the error and transition probabilities, to determine if an error occurs due to the current state's associated BSC, as well as if transitions occur to the previous or next state respectively. The initial condition of the Markov Chain is assumed to be the very first state, $n = 1$.

At the end of each Monte Carlo run, the BER is determined by counting the errors observed and dividing the result by the total number of bits sent. This result is then averaged across all runs, and can be then compared with a reference value. Performing these experiments at different model parameter values and noise levels, allows evaluating the FSMC method's accuracy at various operational scenarios.

The baseline values used in these experiments are the analytical BER values associated with a K-distributed SNR channel, and are utilized as a reference value to compare the simulated BER obtained. In [83], the average BER for K and Rayleigh-Lognormal distributions is studied, with the following result being presented for the former:

$$\bar{P}_b = \frac{1}{2}\left[1 - \frac{\Gamma(\beta + \frac{3}{2})}{(4\alpha^2\gamma)^{\beta+1}\Gamma(\beta+1)} \cdot U\left(\beta + \frac{3}{2}, \beta + 2, \frac{1}{4\alpha^2\gamma}\right)\right], \tag{5.23}$$

where α and β are once again the model's parameters, γ is the average SNR and $U(a, b, z)$ is referred to as the Tricomi function, defined as follows [83]:

$$U(a, b, z) = \frac{1}{\Gamma(a)} \int_0^\infty \mathrm{e}^{-zt} t^{a-1} (1+t)^{b-a-1} \mathrm{d}t. \tag{5.24}$$

This function is also commonly known as the Confluent Hypergeometric function (see equation 4 in section 9.211 of [89]).

5.5 Results and Analysis

Simulation results have been obtained for the Enhanced FSMC-TS model, consisting of an improved version of the FSMC-TS channel proposed by Salamanca et al. [11], in which the B-sector's Rayleigh distribution is replaced with a K-distribution. These results aim to compare the analytical and simulated BER, a key performance metric in a communication system.

Before proceeding with the simulated BER experiment, a visual representation of the CDF equipartitioning performed for each state is presented in figure 5.2. Table 5.1 summarizes the parameters employed to generate these results.

As mentioned previously, the value of α is considered to be equal to 0.5, while the average normalized SNR per symbol and shadowing parameter are set to $\frac{E_s}{N_0} = 3$ [dB] and $\beta = 0.35$

Parameter	Value
α	1
β	0.35
$\frac{E_s}{N_0}$	3 [dB]
K	4

Table 5.1: Parameters employed to illustrate the CDF equipartitioning results.

respectively. $K = 4$ states are employed for the Markov Chain. From figure 5.2, it can be seen that the threshold values calculated allow an effective equipartition of the SNR per symbol, with each state capturing around 0.25 of the CDF, coinciding with the expected result of $\frac{1}{K}$.

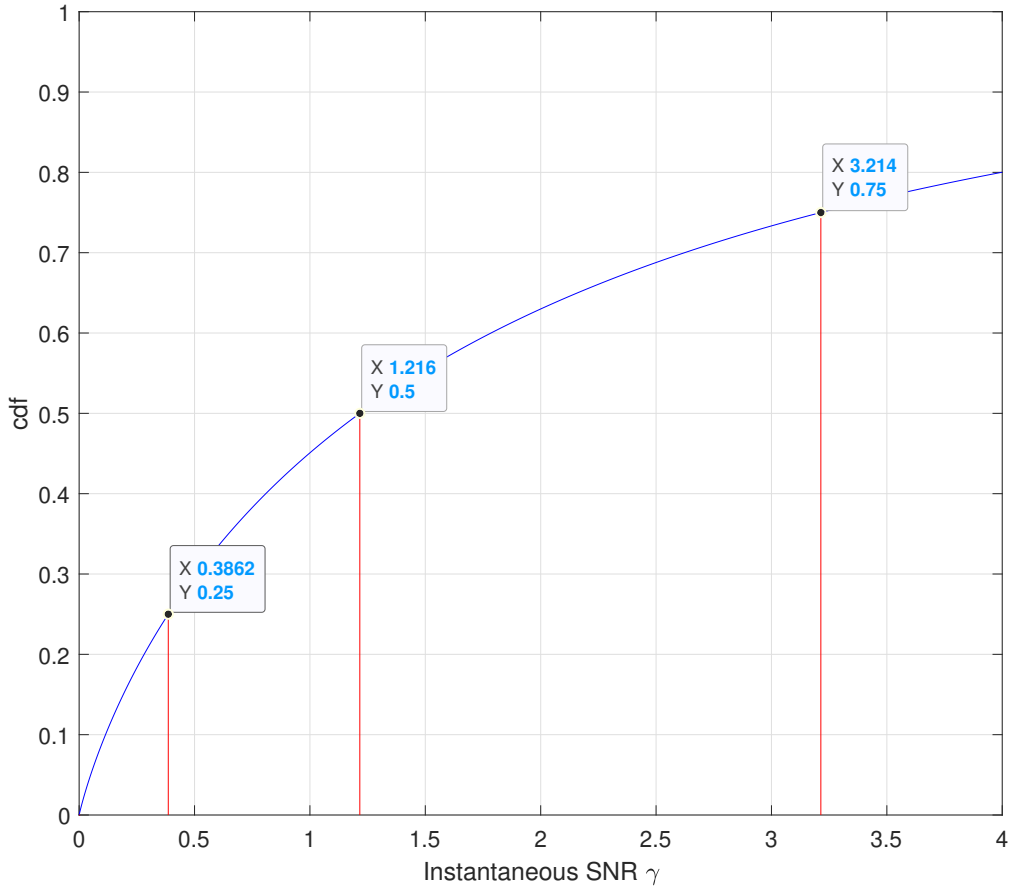

Figure 5.2: K-distribution instantaneous SNR γ CDF after state partitioning.

Following that, Monte Carlo iterations are performed with the Enhanced FSMC-TS model for the B-sector, to obtain an estimate of the simulated BER observed. Table 5.2 summarizes the parameters utilized.

For each of the 400 Monte Carlo iterations, the Markov Chain is simulated for 10^6 [bits]. All other parameters of the communication system are kept identical to what is used in the

Parameter	Value
α	0.5
β	$\{-0.37, 0.35, 2, 5\}$
K	4
Minimum $\frac{E_s}{N_0}$	-10 [dB]
Step $\frac{E_s}{N_0}$	5 [dB]
Maximum $\frac{E_s}{N_0}$	30 [dB]
h	680 [km]
f_c	2.4 [GHz]
θ_c	5°
$\theta_{\max}$	90°

Table 5.2: Markov Chain and orbital parameters used for the Monte Carlo BER Simulations.

original FSMC-TS manuscript by Salamanca et al. [11], with $f_c = 2.4$ [GHz], orbital height $h = 680$ [km], minimum required elevation angle $\theta_c = 5^\circ$ and maximum elevation angle $\theta_{\max} = 90^\circ$.

The Markov Chain parameter set, that is, those described in equations 5.14 through 5.19 are computed as described in section 5.3. Concerning the K-distribution's parameters, the mean signal power Ω is once again set to 1, leading to a value of $\alpha = \frac{1}{2}$ for the instantaneous SNR PDF. Since β characterizes the severity of shadowing present in the channel, values of $\beta \in \{-0.37, 0.35, 2, 5\}$ are used, to illustrate how multiple scenarios can be represented. The normalized average SNR per symbol is varied in steps of 5 [dB], from -10 [dB] to 30 [dB].

Figure 5.3 shows the simulated BER values for different SNR per symbol levels obtained through Monte Carlo simulations, compared with their respective analytical reference value.

Evidently, the inclusion of shadowing in the channel model can cause significant degradation in the observed system performance. The effect is relatively mild for environments with lighter shadowing, with only an additional 1 to 2 [dB] required to maintain a BER of 10^{-2} for $\beta \in \{2, 5\}$. However, in heavily shadowed environments, such as $\beta = -0,37$, this difference in required SNR per symbol increases dramatically, requiring an additional 15 [dB] to maintain a similar BER. Likewise, for a fixed noise level, the BER obtained can increase significantly when going from non-shadowed to heavily shadowed channel conditions. For example, for $E_s/N_0 = 15$ [dB], a BER of around $8 \cdot 10^{-3}$ is obtained for the Rayleigh (unshadowed) channel, while the Enhanced FSMC-TS model with $\beta = -0.37$ (heavily shadowed) exhibits a significantly higher BER, of around $5 \cdot 10^{-2}$.

As seen by both analytical and simulated curves, higher values of β are associated with less prevalent shadowing, with a clear tendency towards the pure Rayleigh scenario (continuous blue curve) when $\beta \to \infty$, consistent with what can be found in literature [86,87]. Conversely, lower values of β, approaching the minimum value of $\beta = -1$ represent more and more heavily shadowed environments. For these values, the BER curves tend to be considerably higher than the unshadowed ones, approaching the BER = 0.5 bound. This corresponds to the behavior outlined in [83], where it is mentioned that the K distribution converges to a Dirac delta function at 0, as $\beta \to -1$.

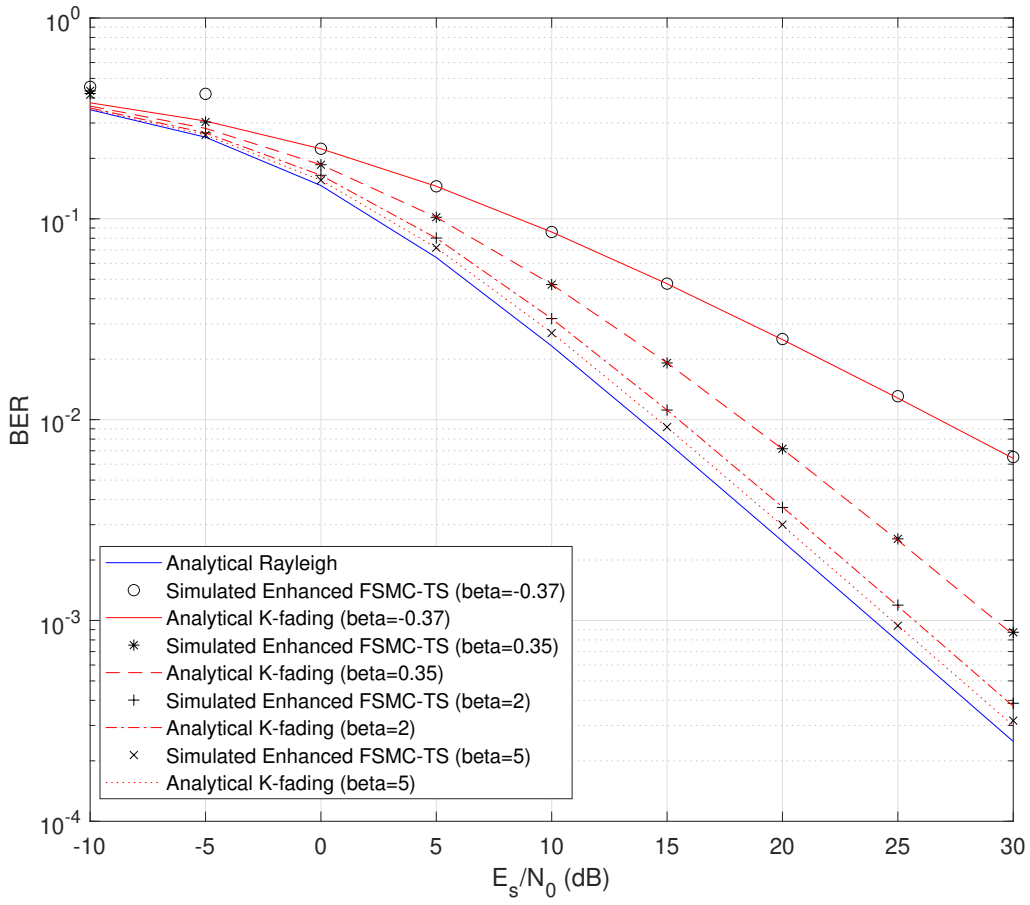

Figure 5.3: Monte Carlo simulation results obtained for the Enhanced FSMC-TS channel model.

With regards to the Enhanced FSMC-TS curve's accuracy to approximate the analytical scenario, good results overall are obtained for high SNR per symbol levels, with little discrepancies found at values above $\frac{E_s}{N_0} = 0$ [dB]. However, the simulated and analytical results show notorious discrepancies at low signal levels, with evident discontinuities found for the FSMC simulated results. Moreover, it can be seen that the SNRs for which the simulations are not accurate approximations depend directly on the selected value of β. For lower values of β, that is, when shadowing is more prevalent, the approximation stops being accurate at higher levels of SNR, while the opposite is true for higher values of β.

Currently, this behavior is attributed to the fact that the error probability for each state is being calculated through numerical integration, as opposed to using an analytical, series-based approach. The latter method is utilized both in the original FSMC-TS manuscript [11] as well as in [90] for the simulation of Nakagami channels using Markov Chains, with excellent results. Utilizing a similar approach could eventually yield more accurate results, especially at low SNRs and high values of β for the K-distribution parameters, since threshold values tend to collapse toward $\gamma = 0$ as $\beta \to -1$ and $\frac{E_s}{N_0} \to -\infty$. In the following paragraphs, the groundwork for a potential deduction of the error probability using series representation is

presented, with the potential to solve the inaccuracy problems observed at low SNRs.

In Appendix A of [90], a derivation for the state error probability e_k is presented, arriving at the following set of equations:

$$e_k = \frac{1}{\pi_k}(\varepsilon_{k+1} - \varepsilon_k), \tag{5.25}$$

$$\varepsilon_k = F_\gamma(\Gamma_{n_k})Q(\Gamma_{n_k}) + I_k, \tag{5.26}$$

$$I_k = \int_0^{\sqrt{2\Gamma_{n_k}}} F_\gamma\left(\frac{x^2}{2}\right)\frac{1}{\sqrt{2\pi}}e^{-\frac{x^2}{2}}dx, \tag{5.27}$$

where $k \in [0, ..., K]$ represents a state and Γ_{n_k} corresponds to the k-th threshold of the n-Sector, with $n \in \{B, G\}$. The term $F_\gamma(\cdot)$ corresponds to the CDF of the instantaneous SNR γ, and $Q(\cdot)$ is the well-known Q-function. As these expressions are valid for any distribution, they can be directly used with the K-distribution's CDF, as described in equation 5.10. The problem is essentially reduced to calculating the integral in equation 5.27.

The following series expansion for $K_v(z)$ can be deduced from [89], for $v \notin \mathbb{Z}$:

$$K_v(z) = \frac{\pi\csc(\pi v)}{2}\left[\sum_{k=0}^{\infty}\frac{1}{\Gamma(k-v+1)k!}\left(\frac{z}{2}\right)^{2k-v} - \sum_{k=0}^{\infty}\frac{1}{\Gamma(k+v+1)k!}\left(\frac{z}{2}\right)^{2k+v}\right]. \tag{5.28}$$

Using this series representation for the Modified Bessel function of the second kind present in the K-distribution's instantaneous SNR CDF, makes it possible to analytically calculate I_k. The following expression is obtained for this term:

$$\begin{aligned} I_k =& \frac{1}{2} - Q(\sqrt{2\Gamma_{n_k}}) - \frac{2^{-\beta-1}\pi\csc(\pi(\beta+1))}{\sqrt{4\pi\frac{E_s}{N_0}\alpha^2}\Gamma(\beta+1)}\left[\sum_{k=0}^{\infty}\frac{\gamma\left(\frac{2k+1}{2}, \Gamma_{n_k}\right)}{2^{2k-\beta-1}\Gamma(k-\beta)k!\left(\frac{E_s}{N_0}\alpha^2\right)^{\frac{2k-1}{2}}}\right. \\ &\left. - \sum_{k=0}^{\infty}\frac{\gamma\left(\frac{2k+2\beta+3}{2}, \Gamma_{n_k}\right)}{2^{2k+\beta+1}\Gamma(k+\beta+2)k!\left(\frac{E_s}{N_0}\alpha^2\right)^{\frac{2k+2\beta+1}{2}}}\right] \quad \text{for } \beta \notin \mathbb{Z} \wedge \beta > -1. \end{aligned} \tag{5.29}$$

The full derivation for equation 5.29 is presented in Appendix C.

While the analysis described here is only valid for $\beta \notin \mathbb{Z}$, a similar calculation can be performed utilizing a separate series expansion of $K_v(\cdot)$ for the special case of $v \in \mathbb{Z}$. If this is achieved, it is theoretically possible to implement the Markov Chain model for the K-distribution utilizing this new expression for state error probability e_k, potentially solving the issues encountered at low SNRs. This topic is revisited in section 6.2, covering avenues for improvement and future work.

5.6 Closing Remarks

Despite the inconsistencies discussed previously, the Enhanced FSMC-TS Model successfully incorporates the effect of shadowing in a two-sector Markov Chain-based channel model. The simulation results presented illustrate how the presence of shadowing can lead to significantly harsher channel conditions, with the additional SNR needed to maintain a given BER of 10^{-2} ranging from 1 [dB] to almost 15 [dB], depending on the specific shadowing parameters. Similarly, for a fixed noise level of 15 [dB], the BER obtained is significantly higher, with an increase from $8 \cdot 10^{-3}$ to around $5 \cdot 10^{-2}$. This enhanced model allows for a more realistic representation of the Direct-to-LEO Satellite Channel.

Nevertheless, the issues encountered at lower SNR still persist in the current state of the model. Section 5.5 provides an outline of how a solution may be found by utilizing series representation instead of numerical integration to calculate the state error probabiilty e_k. Overcoming these limitations will allow further testing and evaluation of the Enhanced FSMC-TS Channel model.

Chapter 6

Conclusion and Future Work

6.1 Conclusion

The growing interest in novel IoT applications using LEO nanosatellites has brought attention to some of the inherent challenges of this new paradigm. However, no definitive answer has been provided in the literature to address the matter of channel modeling in DtS-IoT applications supported by LEO nanosatellites. In this work, we have thoroughly reviewed various channel models applicable to LMS systems, and proposed a methodical approach to comparatively evaluate them and determine which model is the most suited for the scenario under study. Additionally, we have proposed an enhancement to one of the reviewed models, resulting in a new channel model named Enhanced FSMC-TS.

With respect to the comparative channel model analysis, the proposed methodology consists of a three-step framework, constructed to take into accounts the specific issues and limitations of LEO nanosatellite-based DtS-IoT. The analysis performed allowed the shortlisting of three potential candidates from the different channel models that were considered, including both classical and contemporary approaches. The selection was made based on a weighted score metric calculated from three qualitative criteria, each addressing a different dimension of the task at hand. Our initial assessment shows that the three most suited candidates are the Akturan [7], Patzold [9] and FSMC-TS [11] models.

Additionally, experimental results have been obtained through Montecarlo simulations, comparing the fading amplitude variation and CDF for two of the three shortlisted models, with Loo's model included as well as a baseline for comparison. These results allowed an exploratory assessment to be performed at a statistical level for each model, illustrating that both the FSMC-TS and Akturan models can represent similar scenarios, with appropriate parameter selection. However, it should be noted that the results presented correspond to a first approach considering a simulation-based analysis of the pre-selected models the scenario studied. Consequently, further experimentation and analysis is required to provide a more definitive answer to the question of channel modeling in DtS-IoT.

The proposed objective of improving an existing channel model was accomplished successfully, as demonstrated by the addition of shadowing to the FSMC-TS model, in the novel

Enhanced FSMC-TS channel model. This was accomplished by substituting the B-sector's Rayleigh distribution with a K-distribution, a well-known Raylegh-Lognormal substitute. The simulation results show a great accuracy of the simulated model with respect to the analytical BER, especially at high SNR per symbol levels ($\frac{E_s}{N_0} > 0$). The resulting channel exhibits significantly degraded performance metrics, with an additional 15 [dB] required to maintain a BER of 10^{-2} in the most heavily-shadowed scenario studied, when compared to its non-shadowed counterpart. Similarly, for a fixed noise level of 15 [dB], the BER obtained is significantly higher, with an increase from $8 \cdot 10^{-3}$ to around $5 \cdot 10^{-2}$ when moving from the non-shadowed to heavily shadowed scenarios respectively. Additionally, the results show that the FSMC implementation of the K-distribution is consistent the literature, particularly with the observed asymptotic behavior of the model with respect to the parameter β.

Nevertheless, the obtained results are not ideal, and include a noticeable anomaly at lower signal levels, across all tested values of β. Said anomaly consists of a discrepancy between the analytical and FSMC simulated BER values, implying that the current implementation of the FSMC model does not represent the analytical channel at low SNR per symbol values, especifically for values of $\frac{E_s}{N_0} > 0$. It is hypothesized that the problem is caused by an estimation error during the computation of the bit error probability for each state. This error, potentially introduced by the numerical integration performed, is exacerbated at low signal levels, due to the inherent nature of the K-distribution. Still, the foundation for a proposed solution for this problem is presented in this work. Said solution consists of using the Modified Bessel function's series representation to determine an analytical expression for e_k.

6.2 Future Work

Regarding future work, there are multiple avenues to explore moving forward. Concerning the comparative analysis of channel models, the addition of Patzold's models in the simulation experiments is proposed as future work, completing step 2 of the proposed framework. Similarly, further analyis of all three pre-selected models through HITL simulations is proposed as well, utilizing BER as the key performance metric to continue with step 3 of the framework. Specifically, the possibility of utilizing experimental LEO satellite channel measurements as a baseline is particularly appealing, directly comparing each candidate model with real-world data. An approach in this vein would make the selected channel considerably more likely to accurately represent the scenario under study.

With respect to the Enhanced FSMC-TS Channel Model, there are once again various directions to explore as future work. First and foremost, the unusual behavior encountered at low SNR levels should be studied in-depth, possibly addressing the matter with a series-based approach for error calculation, as mentioned previously. Additionally, the behavior of the overall Enhanced FSMC-TS system, considering both G and the modified B-sector, should be studied in-depth, since only the latter was covered in this work. Finally, other alternatives to Rayleigh-Lognormal fading could be explored for FSMC implementation as well, such as the Rayleigh-Birnbaum Sanders [73], Rayleigh Inverse Gaussian [72] or the Generalized Rayleigh [75]. Direct comparison with the K-distribution FSMC may be performed via simulations, utilizing BER as the performance metric to determine the most accurate solution to model the shadowing phenomenon.

Bibliography

[1] I. F. Akyildiz and I. Kak, "The Internet of Space Things/CubeSats," *IEEE Network*, vol. 33, no. 5, pp. 212–218, 2019.

[2] J. H. Nord, A. Koohang, and J. Paliszkiewicz, "The Internet of Things: Review and theoretical framework"," *Expert Systems with Applications*, vol. 133, pp. 97 – 108, 2019.

[3] I. Leyva-Mayorga, B. Soret, M. Röper, D. Wübben, B. Matthiesen, A. Dekorsy, and P. Popovski, "LEO Small-Satellite Constellations for 5G and Beyond-5G Communications," *IEEE Access*, vol. 8, pp. 184955–184964, 2020.

[4] J. A. Fraire, S. Céspedes, and N. Accettura, "Direct-To-Satellite IoT - A Survey of the State of the Art and Future Research Perspectives," in *ADHOC-NOW 2019: Ad-Hoc, Mobile, and Wireless Networks*, (Luxembourg, Luxembourg), pp. 241–258, Oct. 2019.

[5] C. Loo, "A Statistical Model for a Land Mobile Satellite Link," *IEEE Transactions on Vehicular Technology*, vol. 34, no. 3, pp. 122–127, 1985.

[6] E. Lutz, D. Cygan, M. Dippold, F. Dolainsky, and W. Papke, "The Land Mobile Satellite Communication Channel-Recording, Statistics, and Channel Model," *IEEE Transactions on Vehicular Technology*, vol. 40, no. 2, 1991.

[7] R. Akturan and W. J. Vogel, "Elevation angle dependence of fading for satellite PCS in urban areas," *Electronics Letters*, vol. 31, pp. 1125–1127, July 1995.

[8] S. H. Hwang, K. J. Kim, J. young Ahn, and K. C. Whang, "Channel model for non-geostationary orbiting satellite system," *IEEE Vehicular Technology Conference*, vol. 1, no. 7, pp. 41–45, 1997.

[9] M. Pätzold, Y. Li, and F. Laue, "A study of a land mobile satellite channel model with asymmetrical Doppler power spectrum and lognormally distributed line-of-sight component," *IEEE Transactions on Vehicular Technology*, vol. 47, no. 1, pp. 297–310, 1998.

[10] C. Kourogiorgas, M. Kvicera, D. Skraparlis, T. Korinek, V. K. Sakarellos, A. D. Panagopoulos, and P. Pechac, "Modeling of first-order statistics of the MIMO dual polarized channel at 2 GHz for land mobile satellite systems under tree shadowing," *IEEE Transactions on Antennas and Propagation*, vol. 62, no. 10, pp. 5410–5415, 2014.

[11] J. J. Lopez-Salamanca, L. O. Seman, M. D. Berejuck, and E. A. Bezerra, "Finite-State Markov Chains Channel Model for CubeSats Communication Uplink," *IEEE Transactions on Aerospace and Electronic Systems*, vol. 56, no. 1, pp. 142–154, 2020.

[12] M. S. Karaliopoulos and F. N. Pavlidou, "Modelling the Land Mobile Satellite channel: A review," *Electronics and Communication Engineering Journal*, vol. 11, no. 5, pp. 235–248, 1999.

[13] N. Saeed, A. Elzanaty, H. Almorad, H. Dahrouj, T. Y. Al-Naffouri, and M. S. Alouini, "CubeSat Communications: Recent Advances and Future Challenges," *IEEE Communications Surveys and Tutorials*, vol. 22, no. 3, pp. 1839–1862, 2020.

[14] B. Elbert, *Introduction to Satellite Communication*. Artech House, 2008.

[15] D. Roddy, *Satellite Communications*. Professional Engineering, McGraw-Hill Education, 2006.

[16] R. Cochetti, *Mobile Satellite Communications Handbook*. Wiley, 2014.

[17] O. Kodheli, E. Lagunas, N. Maturo, S. K. Sharma, B. Shankar, J. F. M. Montoya, J. C. M. Duncan, D. Spano, S. Chatzinotas, S. Kisseleff, J. Querol, L. Lei, T. X. Vu, and G. Goussetis, "Satellite Communications in the New Space Era: A Survey and Future Challenges," *IEEE Communications Surveys Tutorials*, vol. 23, no. 1, pp. 70–109, 2021.

[18] Earth Observatory, National Aeronautics and Space Administration, "Catalog of Earth Satellite Orbits," 2009. Available at `https://earthobservatory.nasa.gov/features/OrbitsCatalog` (visited on 15-Oct-2021).

[19] Y. Su, Y. Liu, Y. Zhou, J. Yuan, H. Cao, and J. Shi, "Broadband LEO Satellite Communications: Architectures and Key Technologies," *IEEE Wireless Communications*, vol. 26, no. 2, pp. 55–61, 2019.

[20] T. Pratt and J. Allnutt, *Satellite Communications*. Wiley, 2019.

[21] S. Chatzinotas, S. Sharma, and P. Arapoglou, *Satellite Communications in the 5G Era*. IET, 2018.

[22] Z. Qu, G. Zhang, H. Cao, and J. Xie, "LEO Satellite Constellation for Internet of Things," *IEEE Access*, vol. 5, pp. 18391–18401, 2017.

[23] J. J. Khalife and Z. M. Kassas, "Receiver Design for Doppler Positioning with LEO Satellites," in *ICASSP 2019 - 2019 IEEE International Conference on Acoustics, Speech and Signal Processing (ICASSP)*, pp. 5506–5510, 2019.

[24] Z. Kassas, J. Morales, and J. Khalife, "New-Age Satellite-Based Navigation–STAN: Simultaneous Tracking and Navigation with LEO Satellite Signals," *Inside GNSS Magazine*, vol. 14, no. 4, pp. 56–65, 2019.

[25] Z. Z. Kassas, J. Khalife, and M. Neinavaie, "The First Carrier Phase Tracking and Po-

sitioning Results with Starlink LEO Satellite Signals," *IEEE Transactions on Aerospace and Electronic Systems*, pp. 1–1, 2021.

[26] F. Tang, H. Zhang, and L. T. Yang, "Multipath Cooperative Routing with Efficient Acknowledgement for LEO Satellite Networks," *IEEE Transactions on Mobile Computing*, vol. 18, no. 1, pp. 179–192, 2019.

[27] B. Zhao, G. Ren, and H. Zhang, "Multisatellite cooperative random access scheme in Low Earth Orbit satellite networks," *IEEE Systems Journal*, vol. 13, no. 3, pp. 2617–2628, 2018.

[28] W. Wang, Y. Tong, L. Li, A.-A. Lu, L. You, and X. Gao, "Near Optimal Timing and Frequency Offset Estimation for 5G Integrated LEO Satellite Communication System," *IEEE Access*, vol. 7, 2019.

[29] Y. Qian, L. Ma, and X. Liang, "Symmetry Chirp Spread Spectrum Modulation Used in LEO Satellite Internet of Things," *IEEE Communications Letters*, vol. 22, no. 11, pp. 2230–2233, 2018.

[30] L. You, K.-X. Li, J. Wang, X. Gao, X.-G. Xia, and B. Ottersten, "Massive MIMO Transmission for LEO Satellite Communications," *IEEE Journal on Selected Areas in Communications*, vol. 38, no. 8, pp. 1851–1865, 2020.

[31] C. Kourogiorgas and A. D. Panagopoulos, "A rain-attenuation stochastic dynamic model for LEO satellite systems above 10 GHz," *IEEE Transactions on Vehicular Technology*, vol. 64, no. 2, pp. 829–834, 2014.

[32] S.-Y. Li and C. Liu, "Modeling the effects of ionospheric scintillations on LEO satellite communications," *IEEE communications letters*, vol. 8, no. 3, pp. 147–149, 2004.

[33] L. Fernandez, J. A. Ruiz-De-Azua, A. Calveras, and A. Camps, "Assessing LoRa for satellite-to-earth communications considering the impact of ionospheric scintillation," *IEEE access*, vol. 8, pp. 165570–165582, 2020.

[34] E. Juan, M. Lauridsen, J. Wigard, and P. E. Mogensen, "A Time-correlated Channel State Model for 5G New Radio Mobility Studies in LEO Satellite Networks," in *2021 IEEE 93rd Vehicular Technology Conference (VTC2021-Spring)*, pp. 1–5, 2021.

[35] F. Davoli, C. Kourogiorgas, M. Marchese, A. Panagopoulos, and F. Patrone, "Small satellites and CubeSats: Survey of structures, architectures, and protocols," *International Journal of Satellite Communications and Networking*, vol. 37, no. 4, pp. 343–359, 2019.

[36] T. Ferrer, S. Céspedes, and A. Becerra, "Review and evaluation of MAC protocols for satellite IoT systems using nanosatellites," *Sensors (Switzerland)*, vol. 19, no. 8, pp. 1–29, 2019.

[37] A. A. Doroshkin, A. M. Zadorozhny, O. N. Kus, V. Y. Prokopyev, and Y. M. Prokopyev, "Experimental Study of LoRa Modulation Immunity to Doppler Effect in CubeSat Radio

Communications," *IEEE Access*, vol. 7, pp. 75721–75731, 2019.

[38] N. Ye, J. Yu, A. Wang, and R. Zhang, "Help from space: grant-free massive access for satellite-based IoT in the 6G era," *Digital Communications and Networks*, 2021.

[39] D. Li, S. Wu, Y. Wang, J. Jiao, and Q. Zhang, "Age-Optimal HARQ Design for Freshness-Critical Satellite-IoT Systems," *IEEE Internet of Things Journal*, vol. 7, no. 3, pp. 2066–2076, 2020.

[40] M. Bacco, M. Colucci, and A. Gotta, "Application protocols enabling internet of remote things via random access satellite channels," in *2017 IEEE International Conference on Communications (ICC)*, pp. 1–6, IEEE, 2017.

[41] M. Bacco, L. Boero, P. Cassará, M. Colucci, A. Gotta, M. Marchese, and F. Patrone, "IoT applications and services in space information networks," *IEEE Wireless Communications*, vol. 26, no. 2, pp. 31–37, 2019.

[42] J. Wei, J. Han, and S. Cao, "Satellite IoT edge intelligent computing: A research on architecture," *Electronics (Switzerland)*, vol. 8, no. 11, 2019.

[43] S. K. Routray, A. Javali, A. Sahoo, K. P. Sharmila, and S. Anand, "Military Applications of Satellite Based IoT," in *2020 Third International Conference on Smart Systems and Inventive Technology (ICSSIT)*, pp. 122–127, 2020.

[44] S. Kota and G. Giambene, "Satellite 5G: IoT use case for rural areas applications," in *Proceedings of the Eleventh International Conference on Advances in Satellite and Space Communications-SPACOMM*, pp. 24–28, 2019.

[45] Y. Lee and J. P. Choi, "Performance Evaluation of High-Frequency Mobile Satellite Communications," *IEEE Access*, vol. 7, pp. 49077–49087, 2019.

[46] X. Lu, I. H. Kim, A. Xhafa, J. Zhou, and K. Tsai, "Reaching 10-years of battery life for industrial IoT wireless sensor networks," in *2017 Symposium on VLSI Circuits*, pp. C66–C67, 2017.

[47] A. Toorian, K. Diaz, and S. Lee, "The CubeSat Approach to Space Access," in *2008 IEEE Aerospace Conference*, pp. 1–14, 2008.

[48] N. Raissouni, S. E. Adib, J. A. Sobrino, N. B. Achhab, A. Chahboun, A. Azyat, and M. Lahraoua, "Towards LST split-window algorithm FPGA implementation for CubeSats on-board computations purposes," *International Journal of Remote Sensing*, vol. 40, no. 5-6, pp. 2435–2450, 2019.

[49] A. H. Irfan, N. Al-Dhahir, and J. E. Hershey, "Doppler Characterization for LEO Satellites," *IEEE Transactions on Communications*, vol. 46, no. 3, pp. 309–313, 1998.

[50] N. Bohra, H. De Meer, and A. A. Memon, "Analysing the Orbital Movement and Trajectory of LEO (Low Earth Orbit) Satellite Relative to Earth Rotation," in *Personal Satellite Services*, (Berlin, Heidelberg), pp. 1–11, Springer Berlin Heidelberg, 2009.

[51] T. Henderson and R. Katz, "Network simulation for LEO satellite networks," in *18th International Communications Satellite Systems Conference and Exhibit*, pp. 1120–1130, American Institute of Aeronautics & Astronautics, 2000.

[52] M. R. Palattella and N. Accettura, "Enabling Internet of Everything Everywhere: LP-WAN with Satellite Backhaul," in *2018 Global Information Infrastructure and Networking Symposium (GIIS)*, pp. 1–5, 2018.

[53] J. A. Fraire, S. Henn, F. Dovis, R. Garello, and G. Taricco, "Sparse satellite constellation design for LoRa-based direct-to-satellite Internet of things," in *GLOBECOM 2020-2020 IEEE Global Communications Conference*, pp. 1–6, IEEE, 2020.

[54] O. Kodheli, S. Andrenacci, N. Maturo, S. Chatzinotas, and F. Zimmer, "Resource Allocation Approach for Differential Doppler Reduction in NB-IoT over LEO Satellite," in *2018 9th Advanced Satellite Multimedia Systems Conference and the 15th Signal Processing for Space Communications Workshop (ASMS/SPSC)*, pp. 1–8, 2018.

[55] J.-B. Doré and V. Berg, "Turbo-FSK: A 5G NB-IoT Evolution for LEO satellite networks," in *2018 IEEE Global Conference on Signal and Information Processing (GlobalSIP)*, pp. 1040–1044, 2018.

[56] O. Kodheli, N. Maturo, S. Chatzinotas, S. Andrenacci, and F. Zimmer, "NB-IoT via LEO satellites: An efficient resource allocation strategy for uplink data transmission," *IEEE Internet of Things Journal*, pp. 1–1, 2021.

[57] G. Sadeque, S. C. Mohonta, and F. Ali, "Modeling and characterization of different types of fading channel," *International Journal of Science, Engineering and Technology Research*, vol. 4, no. 5, pp. 1410–1415, 2015.

[58] M. Simon and M. Alouini, *Digital Communication over Fading Channels*. Wiley Series in Telecommunications and Signal Processing, Wiley, 2005.

[59] P. Massoud Salehi and J. Proakis, *Digital Communications*. McGraw-Hill Education, 2007.

[60] M. Pätzold, *Mobile Radio Channels*. Wiley, 2011.

[61] A. Goldsmith, *Wireless Communications*. Cambridge University Press, 2005.

[62] M. Hata, "Empirical formula for propagation loss in land mobile radio services," *IEEE transactions on Vehicular Technology*, vol. 29, no. 3, pp. 317–325, 1980.

[63] N. Amitay, "Modeling and computer simulation of wave propagation in lineal line-of-sight microcells," *IEEE Transactions on Vehicular Technology*, vol. 41, no. 4, pp. 337–342, 1992.

[64] P. Bello, "Aeronautical Channel Characterization," *IEEE Transactions on Communications*, vol. 21, no. 5, pp. 548–563, 1973.

[65] A. Neul, J. Hagenauer, W. Papke, F. Dolainsky, and F. Edbauer, "Aeronautical channel characterization based on measurement flights," in *GLOBECOM'87- Global Telecommunications Conference, Tokyo, Japan*, 1987.

[66] D. Cox, "910 MHz Urban Mobile Radio Propagation: Multipath Characteristics in New York City," *IEEE Transactions on Communications*, vol. 21, no. 11, pp. 1188–1194, 1973.

[67] S. O. Rice, "Mathematical analysis of random noise," *The Bell System Technical Journal*, vol. 23, no. 3, pp. 282–332, 1944.

[68] R. Hoppe, G. Wolfle, and F. Landstorfer, "Measurement of building penetration loss and propagation models for radio transmission into buildings," in *Gateway to 21st Century Communications Village. VTC 1999-Fall. IEEE VTS 50th Vehicular Technology Conference (Cat. No.99CH36324)*, vol. 4, 1999.

[69] S. Seidel, T. Rappaport, M. Feuerstein, K. Blackard, and L. Grindstaff, "The impact of surrounding buildings on propagation for wireless in-building personal communications system design," in *[1992 Proceedings] Vehicular Technology Society 42nd VTS Conference - Frontiers of Technology*, 1992.

[70] V. Erceg, L. Greenstein, S. Tjandra, S. Parkoff, A. Gupta, B. Kulic, A. Julius, and R. Bianchi, "An empirically based path loss model for wireless channels in suburban environments," *IEEE Journal on Selected Areas in Communications*, vol. 17, no. 7, pp. 1205–1211, 1999.

[71] A. J. Coulson, A. G. Williamson, and R. G. Vaughan, "A statistical basis for lognormal shadowing effects in multipath fading channels," *IEEE Transactions on Communications*, vol. 46, no. 4, pp. 494–502, 1998.

[72] R. Agrawal, "On efficacy of Rayleigh-inverse Gaussian distribution over K-distribution for wireless fading channels," *Wireless Communications and Mobile Computing*, vol. 7, no. 1, pp. 1–7, 2007.

[73] E. Gomez-Deniz and L. Gómez, "The rayleigh birnbaum saunders distribution: A general fading model," *Symmetry*, vol. 12, no. 3, p. 389, 2020.

[74] L. C. Ozelim, U. S. Dias, and P. N. Rathie, "Revisiting the Lognormal Modelling of Shadowing Effects during Wireless Communications by Means of the α-μ/α-μ Composite Distribution," *Modelling*, vol. 2, no. 2, pp. 197–209, 2021.

[75] E. Gómez-Déniz and L. Gómez-Déniz, "A generalisation of the Rayleigh distribution with applications in wireless fading channels," *Wireless Communications and Mobile Computing*, vol. 13, no. 1, pp. 85–94, 2013.

[76] A. Abdi and M. Kaveh, "K distribution: An appropriate substitute for Rayleigh-lognormal distribution in fading-shadowing wireless channels," *Electronics Letters*, vol. 34, no. 9, pp. 851–852, 1998.

[77] I. Ali, N. Al-Dhahir, and J. E. Hershey, "Predicting the visibility of LEO satellites," *IEEE Transactions on Aerospace and Electronic Systems*, vol. 35, no. 4, pp. 1183–1190, 1999.

[78] W. Li, C. L. Law, V. K. Dubey, and J. Ong, "Ka-band land mobile satellite channel model incorporating weather effects," *IEEE Communications letters*, vol. 5, no. 5, pp. 194–196, 2001.

[79] G. E. Corazza and F. Vatalaro, "A statistical model for land mobile satellite channels and its application to nongeostationary orbit systems," *IEEE Transactions on vehicular technology*, vol. 43, no. 3, pp. 738–742, 1994.

[80] Y. Lee and J. Choi, "Performance analysis of high throughput mobile satellite services (MSS) in high frequency bands," in *34th AIAA International Communications Satellite Systems Conference*, p. 5714, 2016.

[81] H. S. Wang and N. Moayeri, "Finite-State Markov Channel—A Useful Model for Radio Communication Channels," *IEEE Transactions on Vehicular Technology*, vol. 44, no. 1, pp. 163–171, 1995.

[82] T. Núñez, J. López Salamanca, S. Montejo, C. Azurdia, and S. Céspedes, "Analysis of Channel Models for LoRa-based Direct-to-Satellite IoT Networks Served by LEO Nanosatellites," in *2021 IEEE International Conference on Communications Workshops (ICC Workshops)*, pp. 1–6, IEEE, 2021.

[83] A. Abdi and M. Kaveh, "Comparison of DPSK and MSK bit error rates for K and Rayleigh-lognormal fading distributions," *IEEE Communications Letters*, vol. 4, no. 4, pp. 122–124, 2000.

[84] V. Bhaskar, "Finite-state Markov model for lognormal, chi-square (central), chi-square (non-central), and K-distributions," *International Journal of Wireless Information Networks*, vol. 14, no. 4, pp. 237–250, 2007.

[85] H. Pishro-Nik, *Introduction to Probability, Statistics, and Random Processes*. Kappa Research, LLC, 2014.

[86] P. S. Bithas, N. C. Sagias, P. T. Mathiopoulos, G. K. Karagiannidis, and A. Rontogiannis, "Digital communications over generalized-K fading channels," in *2005 2nd International Symposium on Wireless Communication Systems*, pp. 684–687, IEEE, 2005.

[87] P. S. Bithas, N. C. Sagias, P. T. Mathiopoulos, G. K. Karagiannidis, and A. A. Rontogiannis, "On the performance analysis of digital communications over generalized-K fading channels," *IEEE Communications Letters*, vol. 10, no. 5, pp. 353–355, 2006.

[88] W. Jakes, *Microwave Mobile Communications*. New York: Wiley, 1974.

[89] D. Zwillinger and A. Jeffrey, *Table of Integrals, Series, and Products*. Elsevier Science, 2000.

[90] C.-D. Iskander and P. T. Mathiopoulos, "Fast simulation of diversity Nakagami fading channels using finite-state Markov models," *IEEE Transactions on Broadcasting*, vol. 49, no. 3, pp. 269–277, 2003.

Annexes

Annexed A: Instantaneous SNR PDF for K-distribution

The fading amplitude PDF associated with the K-distribution is shown in the equation below:

$$p_K(x) = \frac{2}{\alpha\Gamma(\beta+1)}\left(\frac{x}{2\alpha}\right)^{\beta+1} K_\beta\left(\frac{x}{\alpha}\right). \tag{6.1}$$

Conversely, the following equation is known to define the relationship between fading amplitude x and instantaneous SNR γ:

$$\gamma(x) = x^2\frac{E_s}{N_0}. \tag{6.2}$$

By utilizing the theorem in equation 6.3 along with the two previous equations, an expression can be found for the instantaneous SNR's PDF.

$$f_Y(y) = \begin{cases} \frac{f_X(x_1)}{\|g'(x_1)\|} & \text{where } g(x_1) = y \\ 0 & \text{if } \nexists x \in \mathbb{R} \mid g(x) = y. \end{cases} \tag{6.3}$$

Initially, the derivative of equation 6.2, $\frac{\mathrm{d}}{\mathrm{d}x}\gamma(x)$, must be computed. Due to its polynomial nature, the derivative can be easily determined as shown below:

$$\gamma'(x) = 2x\frac{E_s}{N_0}. \tag{6.4}$$

Additionally, the inverse of $\gamma(x)$ must be calculated, to determine an analytical expression for x_1, such that $\gamma(x_1) = \gamma_1$, whenever such a value of x_1 exists for a given γ_1. Equation 6.5 gives an expression for x, as a function of γ:

$$x(\gamma) = \gamma^{-1}(\gamma) = \sqrt{\frac{\gamma}{\frac{E_s}{N_0}}}. \tag{6.5}$$

Using equations 6.4 and 6.5 in equation 6.3, the following expression can be found for the resulting instantaneous SNR PDF, after some algebraic manipulation:

$$p_K(\gamma) = \frac{2}{\Gamma(\beta+1)} \cdot \gamma^{\frac{\beta}{2}} \left(\frac{1}{4\alpha^2 \frac{Es}{N_0}} \right)^{\frac{\beta+2}{2}} \cdot K_\beta \left[2 \left(\frac{1}{4\alpha^2 \frac{Es}{N_0}} \right)^{\frac{1}{2}} \gamma^{\frac{1}{2}} \right]. \tag{6.6}$$

Annexed B: K-distribution Level Crossing Rate

Using the following equation as a starting point, it is possible to derive an analytical expression of the K-distribution's level crossing rate N_A:

$$N_A = f_m \int_0^\infty \dot{\gamma} \cdot p\left(A, \dot{\gamma}\right) \mathrm{d}\dot{\gamma}.$$

As stated previously, it is assumed that both A and $\dot{\gamma}$ follow the same distribution as the instantaneous SNR γ, in addition to being independent, that is, $p(A, \dot{\gamma}) = p(A)p(\dot{\gamma})$. The auxiliary variables C_A and D are defined as follows:

$$C_A = f_m \frac{4A^{\frac{\beta}{2}}}{\left(\Gamma(\beta+1)\right)^2} \left(\frac{1}{4\alpha^2 \frac{Es}{N_0}} \right)^{\beta+2} \cdot K_\beta \left[2 \left(\frac{1}{4\alpha^2 \frac{Es}{N_0}} \right)^{\frac{1}{2}} \cdot A^{\frac{1}{2}} \right], \tag{6.7}$$

$$D = 2 \cdot \left(\frac{1}{4\alpha^2 \frac{Es}{N_0}} \right)^{\frac{1}{2}}. \tag{6.8}$$

Using these auxiliary variables, it is possible to arrive at the following equation, after replacing the expressions for the PDFs $p(A)$ and $p(\dot{\gamma})$:

$$N_A = C_A \int_0^\infty \dot{\gamma}^{\beta/2} K_\beta \left[D\dot{\gamma}^{1/2} \right] \mathrm{d}\dot{\gamma}. \tag{6.9}$$

With the change of variable $v = D\dot{\gamma}^{1/2}$, the following expression is reached:

$$N_A = \frac{2C_A}{D^{\beta+2}} \int_0^\infty v^{\beta+1} K_\beta[v] \mathrm{d}v. \tag{6.10}$$

The integral in the previous equation has a known analytical solution, as shown in equation 16 of section 6.561 in [89]:

$$\int_0^\infty x^\mu K_v(ax) \mathrm{d}x = 2^{\mu-1} a^{-\mu-1} \Gamma\left(\frac{1+\mu+v}{2} \right) \Gamma\left(\frac{1+\mu-v}{2} \right). \tag{6.11}$$

Using this known result, it is possible to arrive at the final expression for the level crossing rate N_A in a K-distributed model:

$$N_A = 2^{\beta+1} \frac{2C_A}{D^{\beta+2}} \Gamma(\beta+1). \tag{6.12}$$

Finally, to obtain the result shown in equation 5.20, the SNR level A must be replaced with the K thresholds determined for the FSMC.

Annexed C: Error probability using Series Representation

An initial approach for the derivation of the K-distribution state error probability is presented in this appendix, utilizing a series representation for the Modified Bessel function of the second kind, $K_v(\cdot)$. The calculations performed here are only valid for non-integer values of β, but a similar analysis could be performed using a different series representation of $K_v(\cdot)$, valid for integer order values as well.

The relationship between the Modified Bessel functions of first and second kind is described in [89], and presented in the following equation, valid for only non-integer orders v:

$$K_v(x) = \frac{\pi[I_{-v}(x) - I_v(x)]}{2\sin(v\pi)}. \qquad v \notin \mathbb{Z} \tag{6.13}$$

The following series representation is available for $I_v(\cdot)$:

$$I_v(x) = \sum_{k=0}^{\infty} \frac{1}{k!\Gamma(k+v+1}\left(\frac{z}{2}\right)^{2k+v}. \tag{6.14}$$

Utilizing 6.14 in 6.13, it is possible to deduce the following series representation for $K_v(\cdot)$:

$$K_v(z) = \frac{\pi\csc(\pi v)}{2}\left[\sum_{k=0}^{\infty}\frac{1}{\Gamma(k-v+1)k!}\left(\frac{z}{2}\right)^{2k-v} - \sum_{k=0}^{\infty}\frac{1}{\Gamma(k+v+1)k!}\left(\frac{z}{2}\right)^{2k+v}\right], \tag{6.15}$$

which is the series representation mentioned in Chapter 5.

With this series expansion for $K_v(\cdot)$, an analytical expression for the state error probability e_k can be determined. In Appendix A of [90], a derivation is presented, arriving at the following set of equations to calculate e_k:

$$\mathrm{e}_k = \frac{1}{\pi_k}(\varepsilon_{k+1} - \varepsilon_k), \tag{6.16}$$

$$\varepsilon_k = F_\gamma(\Gamma_{n_k})Q(\Gamma_{n_k}) + I_k, \tag{6.17}$$

$$I_k = \int_0^{\sqrt{2\Gamma_{n_k}}} F_\gamma\left(\frac{x^2}{2}\right)\frac{1}{\sqrt{2\pi}}\mathrm{e}^{-\frac{x^2}{2}}\mathrm{d}x. \tag{6.18}$$

As mentioned at the end of Chapter 5, the crux of the matter lies in calculating the integral in Equation 6.18. Replacing the K-distribution instantaneous SNR CDF in this expression, we arrive at the following:

$$I_k = \int_0^{\sqrt{2\Gamma_{n_k}}}\left[1 - \frac{2^{-\beta}}{\Gamma(\beta+1)}\left(\sqrt{\frac{x^2}{2\alpha^2\frac{E_s}{N_0}}}\right)^{\beta+1}\cdot K_{\beta+1}\left(\sqrt{\frac{x^2}{2\alpha^2\frac{E_s}{N_0}}}\right)\right]\cdot\frac{1}{\sqrt{2\pi}}\mathrm{e}^{-\frac{x^2}{2}}\mathrm{d}x, \tag{6.19}$$

where α and β are the K-distribution parameters and $\frac{E_s}{N_0}$ is the normalized SNR.

After algebraic manipulation, and utilizing the Q function's definition $Q(x) = \int_x^\infty \frac{1}{2\pi} \mathrm{e}^{-x^2/2} \mathrm{d}x$, it is possible to arrive at Equation 6.20:

$$I_k = \frac{1}{2} - Q(\sqrt{2\Gamma_{n_k}}) - \underbrace{\int_0^{\sqrt{2\Gamma_{n_k}}} \frac{2^{-\beta}}{\Gamma(\beta+1)} \left(\sqrt{\frac{x^2}{2\alpha^2 \frac{E_s}{N_0}}} \right)^{\beta+1} \cdot K_{\beta+1} \left(\sqrt{\frac{x^2}{2\alpha^2 \frac{E_s}{N_0}}} \right) \cdot \frac{1}{\sqrt{2\pi}} \mathrm{e}^{-\frac{x^2}{2}} \mathrm{d}x}_{J_k} . \tag{6.20}$$

To calculate J_k, the term $K_{\beta+1}(\cdot)$ is replaced with the series expansion of the Modified Bessel function of second kind:

$$\begin{aligned} J_k =& \frac{1}{\sqrt{2\pi}} \int_0^{\sqrt{2\Gamma_{n_k}}} \frac{2^{-\beta}}{\Gamma(\beta+1)} \left(\sqrt{\frac{x^2}{2\alpha^2 \frac{E_s}{N_0}}} \right)^{\beta+1} \frac{\pi \csc(\pi(\beta+1))}{2} \left[\sum_{k=0}^{\infty} \frac{1}{\Gamma(k-\beta)k!} \left(\left(\sqrt{\frac{x^2}{2\alpha^2 \frac{E_s}{N_0}}} \right) \frac{1}{2} \right)^{2k-\beta-1} \right. \\ & \left. - \sum_{k=0}^{\infty} \frac{1}{\Gamma(k+\beta+2)k!} \left(\left(\sqrt{\frac{x^2}{2\alpha^2 \frac{E_s}{N_0}}} \right) \frac{1}{2} \right)^{2k+\beta+1} \right] \mathrm{e}^{-\frac{x^2}{2}} \mathrm{d}x, \end{aligned} \tag{6.21}$$

$$\begin{aligned} =& \frac{2^{-\beta-1} \pi \csc(\pi(\beta+1))}{\sqrt{2\pi}\, \Gamma(\beta+1)} \int_0^{\sqrt{2\Gamma_{n_k}}} \left[\sum_{k=0}^{\infty} \frac{1}{2^{2k-\beta-1}\Gamma(k-\beta)k!} \left(\sqrt{\frac{x^2}{2\alpha^2 \frac{E_s}{N_0}}} \right)^{2k} \right. \\ & \left. - \sum_{k=0}^{\infty} \frac{1}{2^{2k+\beta+1}\Gamma(k+\beta+2)k!} \left(\sqrt{\frac{x^2}{2\alpha^2 \frac{E_s}{N_0}}} \right)^{2k+2\beta+2} \right] \mathrm{e}^{-\frac{x^2}{2}} \mathrm{d}x. \end{aligned} \tag{6.22}$$

Changing the order of integration and summation, the following expression is obtained:

$$\begin{aligned} J_k =& \frac{2^{-\beta-1} \pi \csc(\pi(\beta+1))}{\sqrt{2\pi}\, \Gamma(\beta+1)} \left[\sum_{k=0}^{\infty} \frac{1}{2^{2k-\beta-1}\Gamma(k-\beta)k!} \int_0^{\sqrt{2\Gamma_{n_k}}} \left(\sqrt{\frac{x^2}{2\alpha^2 \frac{E_s}{N_0}}} \right)^{2k} \mathrm{e}^{-\frac{x^2}{2}} \mathrm{d}x \right. \\ & \left. - \sum_{k=0}^{\infty} \frac{1}{2^{2k+\beta+1}\Gamma(k+\beta+2)k!} \int_0^{\sqrt{2\Gamma_{n_k}}} \left(\sqrt{\frac{x^2}{2\alpha^2 \frac{E_s}{N_0}}} \right)^{2k+2\beta+2} \mathrm{e}^{-\frac{x^2}{2}} \mathrm{d}x \right] \end{aligned} \tag{6.23}$$

To solve the two integrals, the change of variable $u = \frac{x^2}{2}$ can be utilized, leading to the following expression:

$$J_k = \frac{2^{-\beta-1}\pi \csc(\pi(\beta+1))}{\sqrt{4\pi\alpha^2\frac{E_s}{N_0}}\Gamma(\beta+1)}\left[\sum_{k=0}^{\infty}\frac{1}{2^{2k-\beta-1}\Gamma(k-\beta)k!}\int_0^{\Gamma_{n_k}}\left(\frac{u}{\alpha^2\frac{E_s}{N_0}}\right)^{\frac{2k-1}{2}}\mathrm{e}^{-u}\mathrm{d}u\right.$$
$$\left.-\sum_{k=0}^{\infty}\frac{1}{2^{2k+\beta+1}\Gamma(k+\beta+2)k!}\int_0^{\Gamma_{n_k}}\left(\frac{u}{\alpha^2\frac{E_s}{N_0}}\right)^{\frac{2k+2\beta+1}{2}}\mathrm{e}^{-u}\mathrm{d}u\right], \tag{6.24}$$
$$= \frac{2^{-\beta-1}\pi \csc(\pi(\beta+1))}{\sqrt{4\pi\alpha^2\frac{E_s}{N_0}}\Gamma(\beta+1)}\left[\sum_{k=0}^{\infty}\frac{1}{2^{2k-\beta-1}\Gamma(k-\beta)k!(\alpha^2\frac{E_s}{N_0})^{\frac{2k-1}{2}}}\int_0^{\Gamma_{n_k}}u^{\frac{2k-1}{2}}\mathrm{e}^{-u}\mathrm{d}u\right.$$
$$\left.-\sum_{k=0}^{\infty}\frac{1}{2^{2k+\beta+1}\Gamma(k+\beta+2)k!(\alpha^2\frac{E_s}{N_0})^{\frac{2k+2\beta+1}{2}}}\int_0^{\Gamma_{n_k}}u^{\frac{2k+2\beta+1}{2}}\mathrm{e}^{-u}\mathrm{d}u\right]. \tag{6.25}$$

The integrals in equation 6.25 can be solved utilizing a well-known result, presented in section 3.351, Eq. 1 of [89], shown in equation 6.26 below:

$$\int_0^w x^{v-1}\mathrm{e}^{-\mu x}\mathrm{d}x = \mu^{-v}\gamma_k(v,\mu w) \quad \mathrm{Re}(v)>0, \tag{6.26}$$

with $\gamma_k(\cdot,\cdot)$ once again defined as the incomplete gamma function. Using this result in equation 6.25 leads to an analytical expression for J_k, described in equation 6.28 below:

$$J_k = \frac{2^{-\beta-1}\pi \csc(\pi(\beta+1))}{\sqrt{4\pi\alpha^2\frac{E_s}{N_0}}\Gamma(\beta+1)}\left[\sum_{k=0}^{\infty}\frac{\gamma_k(\frac{2k+1}{2},\Gamma_{n_k})}{2^{2k-\beta-1}\Gamma(k-\beta)k!(\alpha^2\frac{E_s}{N_0})^{\frac{2k-1}{2}}}\right.$$
$$\left.-\sum_{k=0}^{\infty}\frac{\gamma_k(\frac{2k+2\beta+3}{2},\Gamma_{n_k})}{2^{2k+\beta+1}\Gamma(k+\beta+2)k!(\alpha^2\frac{E_s}{N_0})^{\frac{2k+2\beta+1}{2}}}\right]. \tag{6.27}$$

Replacing this expression for J_k in equation 6.20 leads to the desired result, as shown below:

$$I_k = \frac{1}{2} - Q(\sqrt{2\Gamma_{n_k}}) - \frac{2^{-\beta-1}\pi \csc(\pi(\beta+1))}{\sqrt{4\pi\alpha^2\frac{E_s}{N_0}}\Gamma(\beta+1)}\left[\sum_{k=0}^{\infty}\frac{\gamma_k(\frac{2k+1}{2},\Gamma_{n_k})}{2^{2k-\beta-1}\Gamma(k-\beta)k!(\alpha^2\frac{E_s}{N_0})^{\frac{2k-1}{2}}}\right.$$
$$\left.-\sum_{k=0}^{\infty}\frac{\gamma_k(\frac{2k+2\beta+3}{2},\Gamma_{n_k})}{2^{2k+\beta+1}\Gamma(k+\beta+2)k!(\alpha^2\frac{E_s}{N_0})^{\frac{2k+2\beta+1}{2}}}\right]. \quad \text{for } \beta\notin\mathbb{Z}\wedge\beta>-1 \tag{6.28}$$

As highlighted at the beginning of this Appendix, this derivation is only valid for non-integer values of β, however, it is possible to replicate a similar analysis using the following series expansion for $K_n(\cdot)$, valid only for $n\in\mathbb{Z}$:

$$K_n(z) = \frac{1}{2}\sum_{k=0}^{n-1}(-1)^k \frac{(n-k-1)!}{k!\left(\frac{z}{2}\right)^{n-2k}} + (-1)^{n+1}\sum_{k=0}^{\infty}\frac{\left(\frac{z}{2}\right)^{n+2k}}{k!(n+k)!}\left[\ln\frac{z}{2} - \frac{1}{2}\psi(k+1) - \frac{1}{2}\psi(n+k+1)\right]. \quad (6.29)$$

Annexed D: Source Codes

All MATLAB codes employed can be found in the following GitHub Repository: `https://github.com/tomywofo/thesis_LEO_IoT_channel.git`